OPTIMIZATION OF PURELY SEMICONDUCTING CARBON NANOTUBE COMPLEMENTARY FIELD EFFECT TRANSISTORS

BY

JI HUN KIM

THESIS

Submitted in partial fulfillment of the requirements
for the degree of Master of Science in Electrical and Computer Engineering
in the Graduate College of the
University of Illinois at Urbana-Champaign, 2012

Urbana, Illinois

Advisor:

Professor John A. Rogers

ABSTRACT

Among the remarkable variety of semiconducting nanomaterials that have been discovered, single walled carbon nanotubes (SWNTs) have properties that make them uniquely well suited for high-performance carbon nanotube field-effect transistors (CNTFETs). The most advanced opportunities, however, demand optimized properties of semiconducting SWNTs in horizontal arrays. Here, we present strategies that optimize CNTFETs by using an array-based metallic nanotube removal process with joule heating induced thermocapillary flow in thin organic layers. Detailed experimental studies reveal the selective removal of metallic SWNTs. We provide statistically significant demonstrations to prove the effectiveness and selectivity of this approach and to study the underlying physics of joule-induced thermocapillary flow, and we present several demonstrations of electronic devices based on aligned arrays (both purified and unpurified) along with detailed characterization of their performance.

TABLE OF CONTENTS

CHAPTER 1: INTRODUCTION

The focus of this thesis is the development of methodologies to create thin films of single-walled carbon nanotubes (SWNTs) with properties suitable for advanced electronic applications. Purity of electronic type in SWNT films is key challenge to the field, and the main focus of this thesis.

1.1 SWNT General Properties

Since the discovery of carbon nanotubes (CNTs) in 1991, by Sumio Iijima, their remarkable mechanical, chemical, and physical properties and applications have been researched in many different aspects.[1-5] In particular, their electrical properties (high electronic mobility[5-7] and potential for ballistic transport[8]) make them interesting for applications related to digital[9-11] and RF analog electronic[12-13] devices. SWNTs have been proposed as potential replacements for Si as advances which follow Moore's law become limited.[14,15]

Large variation in properties that exist within a population of SWNTs represents a significant challenge to practical applications. These variations are intrinsic and related to the structure of the specific SWNT. The structure of a SWNT can be thought of as a sheet of graphene cut along a chiral vector and rolled on itself, creating as tube of sp^2 hybridized carbon whose surface is defined by continuous pi bonding, such that the diameter and chirality of the SWNT are defined by the length and direction of the vector, respectively. The practical result is that within any given population of SWNTs, individual SWNTs may have a wide range of properties. Most dramatically SWNTs can be metallic (m-SWNT), semiconducting (s-SWNT), or semi-metallic (sm-SWNT). However, the presence of either in applications which require populations of high purity s-SWNTs can be catastrophic.[16] Among a random population of

SWNTs, roughly 1/3 are expected to be m-SWNTs and 2/3 s-SWNTs. Beyond this almost all other electronic properties have a strong dependence on diameter. Electronic band gap depends on diameter, electronic mobility increases linearly with diameter, and contact resistance increases dramatically for small diameter SWNTs. [5,17] The presence of these variations in electronic type and properties provides limitations for most device demonstration, requiring complex film or device geometries or post-processing techniques.

1.2 Purification of SWNT Films

Many applications of SWNTs require high purity populations with homogeneous electronic type (for the applications here, typically s-SWNT populations are desirable). It is important to consider what degree of purity is required for applications when choosing an approach. For example, most digital electronics require high on/off ratio ($>10^3$-10^4), necessitating >99.9% pure populations, while RF analog devices can tolerate lower on/off (10-100). Furthermore, when considering a purification scheme, it is important that it also be cost-effective, scalable, and not significantly degrade the properties of the SWNTs themselves. The application requirements, effectiveness of the approach, and all of these factors should be considered when evaluating purification techniques. To date, all purification approaches are insufficient in one or several of these areas for many applications. Chapters 2 and 3 discuss details of an alternative approach which is highly effective, scalable, and does not degrade SWNT properties.

1.3 References

1 Avouris, P. Molecular Electronics with Carbon Nanotubes. *Accounts of Chemical Research* **35**, 1026-1034 (2002).

2 Ouyang, M., Huang, J.-L. & Lieber, C. M. Fundamental Electronic Properties and Applications of Single-Walled Carbon Nanotubes. *Accounts of Chemical Research* **35**, 1018-1025 (2002).

3 Popov, V. N. Carbon nanotubes: properties and application. *Materials Science and Engineering: R: Reports* **43**, 61-102 (2004).

4 Charlier, J.-C., Blase, X. & Roche, S. Electronic and transport properties of nanotubes. *Reviews of Modern Physics* **79**, 677-732 (2007).

5 Zhou, X., Park, J.-Y., Huang, S., Liu, J. & McEuen, P. L. Band Structure, Phonon Scattering, and the Performance Limit of Single-Walled Carbon Nanotube Transistors. *Physical Review Letters* **95**, 146805 (2005).

6 Kang, S. J. *et al.* High-performance electronics using dense, perfectly aligned arrays of single-walled carbon nanotubes. *Nat Nano* **2**, 230-236 (2007).

7 Ho, X. *et al.* Scaling Properties in Transistors That Use Aligned Arrays of Single-Walled Carbon Nanotubes. *Nano Letters* **10**, 499-503 (2010).

8 Javey, A., Guo, J., Wang, Q., Lundstrom, M. & Dai, H. Ballistic carbon nanotube field-effect transistors. *Nature* **424**, 654-657 (2003).

9 Cao, Q. *et al.* Medium-scale carbon nanotube thin-film integrated circuits on flexible plastic substrates. *Nature* **454**, 495-500 (2008).

10 Wang, C. *et al.* Extremely Bendable, High-Performance Integrated Circuits Using Semiconducting Carbon Nanotube Networks for Digital, Analog, and Radio-Frequency Applications. *Nano Letters* **12**, 1527-1533 (2012).

11 Javey, A., Wang, Q., Ural, A., Li, Y. & Dai, H. Carbon Nanotube Transistor Arrays for Multistage Complementary Logic and Ring Oscillators. *Nano Letters* **2**, 929-932 (2002).

12 Kocabas, C. *et al.* Radio frequency analog electronics based on carbon nanotube transistors. *Proceedings of the National Academy of Sciences* **105**, 1405-1409 (2008).

13 Nougaret, L. *et al.* 80 GHz field-effect transistors produced using high purity semiconducting single-walled carbon nanotubes. *Applied Physics Letters* **94**, 243505-243503 (2009).

14 Avouris, P., Chen, Z. & Perebeinos, V. Carbon-based electronics. *Nat Nano* **2**, 605-615 (2007).

15 Appenzeller, J. Carbon Nanotubes for High-Performance Electronics: Progress and Prospect. *Proceedings of the IEEE* **96**, 201-211 (2008).

16 Jie Zhang, N. P., Albert Lin, H.-S. Philip Wong, and Subhasish Mitra. in *Proceedings of the Conference on Design, Automation and Test in Europe 2010.* 1159-1164 (European Design and Automation Association).

17 Kim, W. *et al.* Electrical contacts to carbon nanotubes down to 1 nm in diameter. *Applied Physics Letters* **87**, 173101-173103 (2005).

CHAPTER 2: PURIFICATION OF SWNT ARRAYS VIA JOULE-INDUCED THERMOCAPILLARY FLOWS

2.1 Introduction

Among the remarkable variety of semiconducting nanomaterials that have been discovered over the past two decades, the collective properties of single-walled carbon nanotubes (SWNTs) continue to make them uniquely well suited for diverse applications in high performance electronics, sensors and other device technologies. The most advanced opportunities, however, demand perfectly aligned, horizontal arrays of purely semiconducting SWNTs, in chemically pristine forms. We present here strategies that enable this outcome, where nanoscale thermocapillary flows in thin film organic coatings provide means for highly efficient and selective removal of metallic SWNTs from arrays of SWNTs grown by chemical vapor deposition on quartz substrates. The low temperatures and unusual physics associated with this process provide robust, scalable operation, with potential for practical use. Detailed experimental and theoretical studies reveal all of the essential attributes of the underlying thermophysical phenomena. Demonstrations on statistically relevant numbers of transistors quantitatively illustrate the effectiveness of the approach.

Routes to exploit the exceptional electrical properties[1,2] of SWNTs by implementing them in arrays for advanced applications, [3-9] involve extremely challenging requirements on degrees of alignment and purity in semiconducting behavior. Because direct, selective growth of s-SWNTs remains a topic of continuing study, the synthetic strategies that offer the greatest near-term potential fall into two categories: (1) purify the SWNTs and then assemble them into arrays; and (2) assemble the SWNTs into arrays and then purify them. The first has the

advantage that it can exploit recently developed physical-chemical techniques (ultracentrifugation, [10,11] chromatography[12-14] and others[15,16]) for purification. The disadvantages are that SWNTs processed in this way are typically short (~1 μm), chemically modified and/or coated, and difficult to assemble into arrays with high degrees of alignment. [15,17-19] The second overcomes these limitations in assembly through the use of chemical vapor deposition techniques which, when applied on quartz substrates, yield nearly perfectly linear (>99.9% of SWNTs within 0.01˚ of perfect alignment), aligned arrays of long (100 μm and up to ~mm's) and chemically pristine SWNTs. [3,20-23] The main difficulty is in removing the m-SWNTs from arrays of this type. Various techniques attempt to exploit optical, [24] electrical, [25] or chemical[26-28] effects to realize this goal, but they all involve some combination of drawbacks, including incomplete removal of m-SWNTs, degradation of s-SWNTs, inability to operate on aligned arrays and/or reliance on uncertain underlying mechanisms. Among these methods, electrical breakdown is noteworthy because it operates based directly on relevant distinguishing characteristics in charge transport. [25] Here, Joule heating caused by current passing through the m-SWNTs leads to formation of a narrow gap at some point along the length of each of these tubes. During this process, an appropriate electrostatic bias applied to the s-SWNTs minimizes conduction through them and, therefore, the probability of their breakdown. This scheme, however, has two critical disadvantages, each of which renders use in any realistic application impractical. First, breakdown requires high powers (~90 μW/μm for channel lengths > 1 μm, increasing as channel length decreases to values >1 mW/μm). [29-31] Under these conditions, numerous undesirable behaviors in the associated biasing structures (i.e. electrodes, dielectrics) ensue, ranging from shifts in threshold voltage, to avalanche effects, band-to-band tunneling, failure in gate dielectrics, and significant heat sinking at the contacts. These effects create difficulties in

maintaining electrical integrity in the structures and in avoiding transport through the s-SWNTs[20,29,32,33] and therefore degradation in their properties. More significantly, the breakdown process itself only removes the m-SWNTs in isolated, narrow regions (~100 nm lengths), with positions that are not well controlled. [34] In other words, the vast majority of the m-SWNTs remain in the arrays; as a consequence, the resulting arrays are unsuitable for any generalized use in subsequently fabricated devices.

2.2 Thermocapillary-Enhanced Purification

Here, we introduce an approach for eliminating m-SWNTs that offers the key desired attributes, via the use of low temperature thermocapillary effects in thin organic coatings on arrays of SWNTs. We illustrate these concepts through the complete physical removal of all m-SWNTs from linear, horizontally aligned arrays that contain both m-SWNTs and s-SWNTs, without any adverse measurable effects on the latter. Figure 2.1a,b show schematic illustrations and corresponding atomic force microscope (AFM) images of this process, as applied to SWNTs formed by chemical vapor deposition (CVD) on ST-cut quartz substrates with iron nanoparticles as the catalyst and ethanol as the carbon feedstock. The resulting arrays consist of individual, isolated SWNTs, with very few multiwalled nanotubes or bundles of SWNTs, but with a distribution of diameters between ~0.6 and ~2.0 nm and a range of chiralities. [23,31] The key element in the purification process is an ultrathin (~25 nm) amorphous layer of a small molecule organic species, in this example α,α,α'-Tris(4-hydroxyphenyl)-1-ethyl-4-isopropylbenzene, which has been used in the past for other, unrelated lithographic purposes, [35] deposited uniformly over the arrays of SWNTs by thermal evaporation. We refer to this film as a thermocapillary resist (Tc-resist), due to the nature of its operation in the process reported here. Besides its favorable thermophysical properties, as described subsequently in quantitative detail, this

material is well suited for present purposes because it combines hydroxyl and phenyl moieties to facilitate formation of uniform, continuous coatings on the surfaces of both the quartz and the SWNTs. This behavior is critical for its role as an effective etch resist at extremely small thicknesses.

Metal and dielectric layers patterned at the edges of an area of interest enable current injection primarily into only the m-SWNTs, through electrostatically induced increases in the heights and widths of the Schottky barriers that form at the metal contacts at one end of the s-SWNTs. These layers represent a removable, transistor structure in which the gate extends only a small distance beyond the source electrode (~5 μm) compared to the separation between the source and drain (~30 μm) (see Section 2.6). Applying a positive voltage to the gate (typically ~20 V) and a negative voltage to the drain (typically ~40-50 V), while holding the source at electrical ground, leads to selective Joule heating only in the m-SWNTs, due to approximately unipolar p-type behavior in the s-SWNTs. This set of bias conditions produces small increases in temperature in the vicinity of the m-SWNTs, and none at the s-SWNTs. The large thermal gradients associated with the nanoscale localization of these heat sources, in turn, drive mass transport in the Tc-resist via the action of thermocapillary forces. In typical experiments (fields of ~1.33-1.66 V/μm along the SWNTs for 5 min, with substrate heating to 60 ˚C), the resulting material flows yield trenches centered at the positions of the m-SWNTs and extending throughout the thickness of the Tc-resist with widths at the base that we estimate to be ~100 nm. Reactive ion etching (RIE; O_2/CF_4) physically eliminates the m-SWNTs, which are all exposed in this manner, without affecting the s-SWNTs, which remain coated. Removing the Tc-resist and metal/dielectric structures leaves a purified array of SWNTs, consisting only of s-SWNTs, in configurations well suited for planar integration into diverse classes of devices and sensors that

demand, or benefit from, exclusively semiconducting operation. In the following, we refer to this overall process as thermocapillary-enabled purification (TcEP) of arrays of SWNTs.

A key feature of TcEP is its exceptional efficiency in removing the m-SWNTs completely and exclusively. Such operation is important because most envisioned applications of s-SWNTs in electronics, for example, require purity at the level of 99.99% or better (i.e. fewer than one m-SWNT for every 10,000 s-SWNTs). For present purposes, we define a SWNT as metallic (semiconducting) if the ratio between the on (I_{on}) and off (I_{off}) currents (i.e. on/off ratio) in a well designed transistor structure that incorporates this SWNT is less than (greater than) ~100. This definition places SWNTs that are sometimes referred to as quasi-metallic into the m-SWNT classification. (In all cases, we observe a clear distinction between the behavior of m-SWNTs and s-SWNTs defined in this way, for populations of SWNTs grown on quartz. In particular, of the hundreds of SWNTs studied here and elsewhere, none exhibit on/off ratios between ~50 and ~1000.)[36] Detailed electrical characterization (i.e. I_{on} and I_{off} before and after TcEP) and counting statistics (i.e. total numbers of SWNTs before and after) performed on significant numbers of devices (35 devices, each with an active area of ~30×30 μm to enable full visualization by AFM; 377 SWNTs in total) provide quantitative insights into the effectiveness. Figure 2.1c shows a representative transfer characteristic for a device before and after TcEP, measured using the same metal/dielectric structures that enable selective Joule heating. The results illustrate a dramatic reduction in I_{off} (from 0.7 μA to $2\text{x}10^{-5}$ μA), to improve the on/off ratio from 2.7 to $3\text{x}10^{4}$. All devices showed on/off ratios <10 (median=3.7) before and $>2\text{x}10^{3}$ (median=$6.6\text{x}10^{4}$) after TcEP, independent of the number of SWNTs removed (Fig. 2.1d). The relatively small numbers (<30) of SWNTs in each device used to examine the statistics lead to

the conclusion that the observed on/off ratios following TcEP correspond to complete removal (i.e. 100%) of m-SWNTs from the as-grown arrays.

Several other results suggest that the process also preserves most or all of the s-SWNTs. First, of the 377 SWNTs present initially, 63% (i.e. 238 SWNTs) remain after TcEP. This outcome is consistent with the expected percentage (~66%) of s-SWNTs in collections of SWNTs grown by CVD.[3] Second, among 28 devices where the SWNT type can be determined from electrical behaviors measured before and after TcEP (i.e. those devices that incorporate ≤ 2 SWNTs), all of the m-SWNTs and none of the s-SWNTs show trenches (for optimized conditions; see Chapter 3, Fig. 3.1). Third, reductions in I_{on} induced by TcEP are modest; for the example of Fig. 2.1c the ratio of I_{on} after the process to its value before is $I_{on,\,a} / I_{on,\,b}$ ~25%. The weighted average from all of the devices is $I_{on,\,a} / I_{on,\,b}$ ~30%. These results can be interpreted by examining the dependence of $I_{on,\,a} / I_{on,\,b}$ on the percentage of SWNTs removed by TcEP (Fig. 2.1e). The trends are consistent with models that assume 100% preservation of s-SWNTs, expected populations of s-SWNTs and m-SWNTs, and ratios of conductances of m-SWNTs to s-SWNTs (in their on state) that are within an experimentally observed range of 6:1 and 2:1 (see Chapter 3, Fig. 3.3). Collectively, then, all observations are consistent with highly selective and efficient operation in TcEP, in which all m-SWNTs are eliminated, and most or all s-SWNTs are preserved.

2.3 Fundamental Aspects of Joule-Induced Thermocapillary Flow

The thermocapillary effects and the ability to exploit this physics at the nanoscale using remarkably small increases in temperature (a few ˚C) are critical to practical and effective operation of TcEP. Detailed experimental and theoretical studies reveal the quantitative aspects.

We start by examining the distributions of temperature generated during TcEP and their role in the behavior of the Tc-resist. Figure 2.2a shows a scanning Joule expansion microscope (SJEM[37]) image that reveals patterns of thermal expansion that result from Joule heating in an array of SWNT, at a drain-source bias condition $V(t)=V_{DS}\cos(2\pi ft)$ with V_{DS}=5V and f=386 kHz, where associated Joule heating with power density $Q(t)=Q_0\left[1+\cos(4\pi ft)\right]/2$ yields AC thermal expansion at frequency 2f, according to $E(t)=\left[E_1+E_0\cos(4\pi ft)\right]/2$ Here the components including E_1 and E_0 are the DC and AC thermal expansions, respectively. Figure 2.2b shows AFM topographical images of the same array coated with Tc-resist, after application of several different, increasing values of V_{DS} (direct current for 5 min; substrate temperature 60 ˚C). (The image signal corresponds to the peak-peak value of the AC expansion, E_0.) A key observation is that the distributions in expansion, and therefore temperature (Fig. 2.2a), correspond directly to the geometries of trenches that appear in the Tc-resist (Fig. 2.2b). For instance, trenches observed by AFM progressively form with increasing V_{DS} in an order consistent with the relative temperatures of the SWNTs revealed by SJEM; e.g., trenches at the second and fifth SWNT from the right appear first and last, respectively. Related effects can be observed along an individual SWNT, where trenches nucleate in areas of enhanced temperature increase ('hot spots'; arrows in Fig. 2.2a and the top frame of Fig. 2.2b). These indications establish a clear, although qualitative, connection between temperature and operation of the Tc-resist.

The first step to quantitative understanding of TcEP is an experimentally validated model for nanoscale heat flow in this system. Raw data from SJEM measurements indicate relative temperature rises associated with AC Joule heating (V_{DS}=3V, f=30kHz), but not their absolute

values. Figure 2.2c shows a representative cross sectional profile of E_0 for the case of a SWNT with length ~ 3.5 μm, where the power per unit length (power density) is $Q(t) = Q_0\left[1+\cos(4\pi ft)\right]/2$ with Q_0 estimated to be ~13 μW/μm based on the total input power into the device, which includes three SWNTs that yield SJEM signals on an SiO_2/Si substrate, and the corresponding SJEM image (See Chapter 3, Fig. 3.5). Analytical models of temperature distributions associated with Joule heating in a SWNT, treated as a line heat source with length L and an input power density of $Q(t) = Q_0\left[1+\cos(4\pi ft)\right]/2$, can be developed. (see Chapter 3, Fig. 3.6). Boundary conditions involve continuous temperature and heat flow at all material interfaces except those with the SWNT, negligible heat flow at the top surface and a constant temperature at the base of the substrate. For the SWNT interface, discontinuous heat flow, $Q(t)$, is assumed, as a means to introduce the Joule heat source. The results, together with materials constants taken from the literature and analytical treatments of the resulting thermal expansion, yield expansion profiles that have both peak magnitudes (E_0~50 pm) and spatial distributions (characteristic widths ~340 nm) that are remarkably consistent with the SJEM results (~40 pm and ~320 nm, respectively), when Q_0 ~ 13 μW/μm, the estimated experimental value. Figure 2.2d shows the associated AC temperature rises (θ_0) and thermal gradients ($d\theta_0/dx$), such that $\theta(t) = \left[\theta_1 + \theta_0\cos(4\pi ft)\right]/2$ (θ_1 is the DC temperature rise; see Chapter 4 for additional details). When applied to the case of DC heating (f=0), and quartz substrates, the same analytical model yields an expression for the rise in temperature of the surface of the Tc-resist, $\theta = T - T_\infty$ where T_∞ defines the temperature of the background,

$$\theta(x,y)=\frac{1}{2k_s\pi}\int_{-L/2}^{L/2}d\eta\int_0^\infty\frac{Q_0J_0\left(\xi\sqrt{(\eta-y)^2+x^2}\right)}{\cosh\left(\xi h_f\right)+\frac{k_f}{k_s}\sinh\left(\xi h_f\right)}\mathrm{d}\xi \quad (1)$$

Here, k_s and k_f are the thermal conductivity of Tc-resist and quartz substrate, respectively, and h_f is the thickness of Tc-resist. This solution, which is also consistent with 3D finite element analysis (ABAQUS), suggests that experimentally observed power densities needed to achieve trenches in the Tc-resist when on quartz (~3-10 μW/μm per SWNT), yield remarkably small increases in temperature at the SWNTs (~2-5 ˚C). Independent measurements of thermocapillary flows induced by heated AFM tips, where the peak temperatures are measured directly, exhibit similar behaviors (see Chapter 3, Fig. 3.10).

Even these small increases in temperature (~4 ˚C) create large thermal gradients (~20 ˚C/μm), due to the nanoscale dimensions of the sources of heat, defined by the diameters of the SWNTs, ~0.6-2 nm. These gradients are, in fact, sufficient to induce thermocapillary forces capable of driving complete flow of the Tc-resist away from the heated regions (i.e. the m-SWNTs). The detailed physics is critically important for many reasons, one of which is immediately evident from inspection of Figs. 2.2a,b. At large V_{DS} (>1 V/μm), the trenches associated with SWNTs that show pronounced hot spots exhibit uniform widths, with no apparent consequence of spatial non-uniformities in heating. Likewise, SWNTs that show vastly different temperatures at a given V_{DS} display similar trench widths at sufficiently large V_{DS} (>1 V/μm). Figure 2.2e shows results for the second SWNT from the right, extracted from Fig. 2.2a and the bottom frame of Fig. 2.2b. Clearly, the variations (between the mean value and maximum value) in the expansion measured along the length of the SWNT by SJEM are much larger, in fractional sense 10x larger, than those in the trench widths, quantified by separations

between the raised regions of the Tc-resist at the edges of the trench (W_{Tc}). This type of physics provides an ability to realize trenches with small, uniform widths even across large-scale arrays that incorporate m-SWNTs with wide ranges of conductances and diameters, and consequently, peak temperatures and thermal gradients. Figure 2.2f shows the average W_{Tc} for a number of different, individual SWNTs as a function of Q_0. Similar values occur over a wide range of powers (~10-40 μW/μm), even beyond those associated with optimized conditions for TcEP. This behavior is much different than that expected from other thermally driven processes, such as sublimation or ablation, which typically involve abrupt temperature thresholds (See Chapter 3, Fig. 3.13); it is among several quantitative aspects of nanoscale thermocapillary flow that are essential to understanding and optimizing the process.

The governing equation of motion for thermocapillarity in systems where the dimension along the SWNTs can be considered infinite corresponds to unidirectional flow in which the thickness profile in the Tc-resist can be written $h(x,t)$ and

$$\frac{\partial \bar{h}}{\partial \bar{t}} + \frac{\partial}{\partial \bar{x}}\left[\frac{\bar{\tau}\bar{h}^2}{2\bar{\mu}} + \frac{\bar{h}^3}{3\bar{\mu}}\frac{\partial}{\partial \bar{x}}\left(\bar{\gamma}\frac{\partial^2 \bar{h}}{\partial \bar{x}^2}\right)\right] = 0 \qquad (2)$$

where $\bar{h} = h/h_f$, $\bar{x} = x/h_f$, $\bar{t} = \gamma_1 Q_0 t/\left(\mu_0 k_f h_f\right)$, $\bar{\mu} = \mu/\mu_0$, $\bar{\gamma} = k_f\gamma/\left(Q_0\gamma_1\right)$, $\bar{\theta} = k_f\theta/Q_0$, $\bar{\tau} = \partial\bar{\theta}/\partial\bar{x}$ is the thermocapillary stress, μ is viscosity at temperature T, μ_0 is the viscosity at the background temperature $T = T_\infty$, and γ is the surface tension, which often exhibits a linear dependence on temperature (i.e., $\gamma = \gamma_0 - \gamma_1\theta$). Figure 2.3a shows the geometry. The appropriate initial condition is $\bar{h}\left(\bar{x}, \bar{t} = 0\right) = 1$. The boundary conditions are $\bar{h}\left(\bar{x} = \pm\infty, \bar{t}\right) = 1$,

and zero pressure, $\frac{\partial^2 \bar{h}}{\partial \bar{x}^2}(\bar{x} = \pm\infty, \bar{t}) = 0$. With Eq. (1) for the temperature, numerical solutions to this system yield $\bar{h} = h/h_f$, based on assumptions that (a) at each point along *x*, the temperature throughout the thickness of the Tc-resist is equal to the temperature at its interface with the substrate and (b) flow in the Tc-resist does not change the temperature distributions. Figure 2.3b shows results for the case of polystyrene, [38] which exhibits behaviors like the Tc-resist but with less ideal properties (see Chapter 3, Fig. 3.12), and, unlike the Tc-resist, has a known temperature dependent surface tension, according to $\gamma = 50.40 - 0.0738\theta$ mJ/m^2. For this example, $\bar{\mu} = 1$, consistent with the small rise in temperature, and Q_0 = 16.7 μW/μm (from experiment). The trenches gradually widen and deepen with time, as the displaced material forms ridges at the edges. AFM measurements of a representative SWNT coated with Tc-resist, after Joule heating for various time intervals (V_{DS}~0.7 V/μm, 30 ˚C background heating) show similar behaviors and profiles (Fig. 2.3c,d). At longer times, wider trenches result, to the point where SWNTs can be clearly observed at the base in AFM measurements (Fig. 2.3e). Although the specific time durations needed to form complete trenches ($\bar{t}$~1) yield computed values of W_{Tc} that are larger than those observed experimentally, the essential time dependence is captured accurately by the theory. For example, Fig. 2.3f shows the measured time dependence of W_{Tc} for two SWNTs, where both show behavior expected theoretically, namely $W_{Tc} \sim t^{0.25}$ (see Chapter 3, Fig. 3.8-3.9). Another prediction of the theory is that, for a given time *t* = 300 s, the value of W_{Tc} depends only weakly on Q_0, over a remarkably large range; i.e., from ~10 μW/μm to ~35 μW/μm (see Chapter 3, Fig. 3.9). This finding is consistent with observations discussed in the context of Fig. 2.2. Finally, besides capturing the underlying physics, these models also establish a set of guidelines for the selection of optimal materials for Tc-resists, i.e. large

temperature coefficients of surface tension and low viscosities yield narrow trenches within reasonable experimental times. Furthermore, decreasing the thickness reduces the trench widths. Empirical studies of various materials for Tc-resists (see Chapter 3, Fig. 3.12) led to the selection of the molecular glass reported here.

2.4 Large Area TcEP

The envisioned practical use of TcEP is in a preparatory mode, where it serves as one of the several steps, such as substrate cleaning, SWNT growth, transfer and others, that occur before device processing. Such a scheme decouples TcEP from any detailed consideration in component or circuit layout, and is made possible by the ability to eliminate all m-SWNTs, in their entirety, and to do so with removable electrode / dielectric structures. Two approaches can be considered. In the first, one or a small number of sets of electrodes, each with large lateral extent as illustrated in Figure 2.4a,b, enable elimination of m-SWNTs over significant areas. Here processing occurs on hundreds or thousands of SWNTs at once, using pulsed currents to avoid cumulative heating (see Chapter 3, Fig. 3.11). Figure 2.4c shows the electrical characteristics of the structure in Fig. 2.4a before and after TcEP, where, $I_{on,\,a}$ / $I_{on,\,b}$ is ~20% and the on/off ratio after the process is ~$1x10^3$, similar to the results achieved on the small-scale arrays discussed previously. Figure 2.4d illustrates an alternative approach, in which smaller pairs of interconnected electrodes provide for TcEP in distributed regions, lithographically aligned at a coarse level to areas of interest in a final application. Outcomes in this case, in terms of effects on I_{on} and I_{off}, are in the range of those achieved in other geometries.

2.5 Conclusions

In summary, the TcEP method introduced here provides scalable and efficient means for converting heterogeneous arrays of SWNTs into those with purely semiconducting character. Careful control of the process might also allow refined forms of purification, based not just on differences between m-SWNTs and s-SWNTs, but on differences in threshold voltages or other more subtle characteristics among the s-SWNTs themselves. Other promising opportunities for future work include development of optimized conditions and materials for performing TcEP directly on high density arrays (e.g. >10 SWNT/μm), and of schemes that eliminate the need for electrode structures, using electromagnetic exposures or other processes that can take advantage of the unique and low temperature operation of nanoscale thermocapillary flows.

2.6 Methods

Forming horizontally aligned arrays of SWNTs. Photolithography (AZ 5214 positive photoresist), electron beam evaporation (0.6 nm Fe; AJA), and subsequent liftoff defined regions of catalyst in the geometry of strips oriented perpendicular to the preferred growth direction on ST-cut quartz substrates (Hoffman). Annealing at 950 ˚C for 1 hr (quartz tube furnace with ~1 inch outer diameter), cooling the furnace, purging it with hydrogen, and then heating to 925 ˚C prepared the iron catalyst for chemical vapor deposition. Introduction of growth gases (20 sccm H_2, 20 sccm Ar, bubbled through ethanol) at 925 ˚C for 20 min yielded well aligned arrays of SWNTs.

Fabricating source, drain, gate and gate dielectric structures. Photolithography, electron beam evaporation (2 nm Ti, 48 nm Pd; AJA) and liftoff defined source and drain electrodes (channel length, *L*, of 30 μm, and with various channel widths, *W*). Photolithography (AZ 5214)

and reactive ion etching (100 mtorr, 20 sccm O_2, 100 W, 30 s; Plasma-Therm RIE) removed SWNTs everywhere except for regions between these electrodes. Prebaking (250 ˚C, 2 hr, in a glove box) a spin cast (4000 rpm, 60 s) solution to a spin-on glass (SOG; Filmtronics; methylsiloxanes 215F, 15:1 diluted in IPA)[39] and then curing the material formed films of SOG (35 nm) uniformly across the substrate. Atomic layer deposition (80 ˚C; Cambridge NanoTech) created films of Al_2O_3 (30 nm) on top of the SOG. Photolithography (AZ 5214) and etching (6:1 BOE for 50 s, followed by rinsing for 5 min in deionized water) removed most of the SOG/Al_2O_3 bilayer between the source/drain electrodes, to expose substantial lengths of the SWNTs in the region between the source and drain (i.e. ~15-20 μm). Prebaking (110 ˚C, 10 min) a spin cast 5wt% solution of polyvinyl alcohol (PVA; M_w between 89,000 and 98,000, 99%, hydrolyzed, Sigma-Aldrich; solvent: D.I. water) mixed with photosensitizer (ammonium dichromate), >99.5%, Sigma-Aldrich, PVA: photosensitizer=40:1 (weight ratio)[40] (800 rpm, 60 s spread cycle, 4000 rpm, 60 s spin cycle) followed by photolithographic patterning and postbaking (110 ˚C, 30 min) defined a layer of PVA (~400 nm) on top of and aligned with the SOG/Al_2O_3 bilayer. Photolithography (AZ 5214), electron beam evaporation (50 nm Ti or Cr), and lift-off defined a gate electrode on top of this dielectric stack.

Fabricating devices that incorporate a single SWNT. The fabrication procedures followed those described above. The use of arrays of SWNT grown at low density (0.1-0.2 SWNT/μm), and subsequently etched in patterns that removed all of the SWNTs except those in narrow strips (~3 μm widths) yielded devices with small numbers of SWNTs. Electrical and AFM analyses identified a subset of such devices that incorporated only a single SWNT bridging the source and drain electrodes.

Thermocapillary flow and etching to remove m-SWNTs. Thermal evaporation (0.5 Å/s, Kurt Lesker) formed thin layers (25 nm) of α,α,α'-Tris(4-hydroxyphenyl)-1-ethyl-4-isopropylbenzene (TCI international) as the Tc-resist. Applying a voltage between the source/drain electrodes (V_{DS} = -40 to -50 V, corresponding to fields of -1.33 to -1.66 V/μm) while biasing the source/gate to +20 V under vacuum (~1×10^{-4} torr, Lakeshore) and holding the substrate temperature at 60 ˚C, all for ~5 min, yielded trenches in the Tc-resist at the locations of the m-SWNTs. Reactive ion etching (10 mtorr, 1 sccm O_2, 1 sccm CF_4, 75 W, 20 s; Plasma-Therm RIE) eliminated the m-SWNTs exposed in this manner, without affecting the s-SWNTs. Immersion in acetone for 30 min removed the Tc-resist, to complete the process.

Scanning Joule Expansion Microscopy. Devices were wire bonded to a sample holder (Spectrum Semiconductor Materials) to allow contact mode AFM scanning (Asylum MFP 3D and Cantilever Asylum # Olympus AC240TS) while applying suitable biases to the electrode structures. Evaluation of the force/displacement curve for the cantilever prior to scanning defined the relationship between deflection and detector signal. A function generator (Agilent 33250A) provided the AC bias and the reference signal for the lock-in amplifier (Stanford SR844). The lock-in amplifier collected the amplitude and phase of the signal associated with the thermal expansion of the substrate which occurred at twice the frequency of the applied electrical bias. For SJEM of SWNTs on quartz substrate, thermal evaporation formed thick layers (~100 nm) of Tc-resist on devices consisting of arrays of SWNTs between two electrodes (i.e. two-terminal devices, with L=30 μm, W=30 μm). The bias consisted of a sinusoidal voltage with amplitude of 5 V and frequency of 386 kHz. For SJEM of SWNTs on SiO_2 (200 nm) / Si, the sample consisted of a two-terminal device with a spin cast overcoat of poly(methylmethacrylate) (PMMA; Microchem. 950 A2) with thickness of ~120 nm. The bias consisted of a sinusoidal

voltage with amplitude of 3V and frequency of 30 kHz. The doped silicon substrate was electrically grounded.

Studying the kinetics of trench formation. Thermal evaporation deposited thin layers of Tc-resist (~25 nm) on two-terminal devices (L=30 μm, W=100 μm) configured for electrical connection while in the AFM (Asylum research ORCA sample mount). Images collected by fast scanning (~30 s acquisition times) defined the topography of a small region of interest. In between scans, application of electrical biases for durations short compared to the normalized flow rates (0.1 s at short times and increasing to 30 min at long times) caused the trenches to increase in width by controlled amounts. A total of ~400 scans, corresponding to the device under bias for a total, accumulated time of ~8 hr, revealed the kinetics of trench formation, throughout and well beyond the time of interest for TcEP. The data enabled quantitative validation of models of thermocapillary flow. Detailed analysis allowed for accurate extraction of the average trench widths, and complete surface profiles, as a function of time.

Removing the gate electrode and dielectric. Following TcEP, the purified SWNTs (i.e. consisting only of s-SWNTs) were protected by a patterned layer of photoresist (AZ 5214) prior to removal of the gate metal (for Ti, Transene, Inc.; titanium etchant TFTN; for Cr, Transene, Inc.; chrome mask ethant-CE-5M 9). Wet etching (H_2SO_4:H_2O_2=2:1, 60 ˚C, 5 ~10 s) removed the cross-linked PVA. Etching in buffered hydrofluoric acid (BOE 6:1, 30 s) removed the SOG/Al_2O_3 bilayer. Stripping the photoresist completed the process.

Finite element modeling of thermal effects. The 3D finite element model for the temperature distributions used eight-node, hexahedral brick elements in a finite element software package (ABAQUS) to discretize the geometry. The SWNT was treated as a volume heat source, with a

zero heat flux boundary at the top surface of Tc-resist, and a constant temperature T_∞ at the bottom of the quartz substrate.

Numerical modeling of thermocapillary flows. The equations of motion represent a pair of coupled partial differential equations $\frac{\partial \bar{h}_1}{\partial \bar{t}} = \frac{\partial}{\partial \bar{x}}\left(-\frac{\bar{\tau}\bar{h}_1^2}{2\bar{\mu}} - \frac{\bar{h}_1^3}{3\bar{\mu}}\frac{\partial \bar{\gamma}}{\partial \bar{x}}\bar{h}_2 - \frac{\bar{h}_1^3\bar{\gamma}}{3\bar{\mu}}\frac{\partial \bar{h}_2}{\partial \bar{x}} \right)$ and $\frac{\partial^2 \bar{h}_1}{\partial \bar{x}^2} - \bar{h}_2 = 0$ where $\bar{h}_1 = \bar{h}$. The boundary conditions are $\bar{h}_1\left(\bar{x}, \bar{t} = 0\right) = 1$ $\bar{h}_2\left(\bar{x}, \bar{t} = 0\right) = 0$, $\bar{h}_1\left(\bar{x} = \pm\infty, \bar{t}\right) = 1$ and $\bar{h}_2\left(\bar{x} = \pm\infty, \bar{t}\right) = 0$. A Fortran routine (PDE_1D_MG) was used to solve these two partial differential equations directly.

2.7 References

1 Franklin, A. D., Lin, A., Wong, H. S. P. & Chen, Z. Current Scaling in Aligned Carbon Nanotube Array Transistors With Local Bottom Gating. *Electron Device Letters, IEEE* **31**, 644-646 (2010).

2 Zhou, X., Park, J.-Y., Huang, S., Liu, J. & McEuen, P. L. Band Structure, Phonon Scattering, and the Performance Limit of Single-Walled Carbon Nanotube Transistors. *Physical Review Letters* **95**, 146805 (2005).

3 Kang, S. J. *et al.* High-performance electronics using dense, perfectly aligned arrays of single-walled carbon nanotubes. *Nat Nano* **2**, 230-236 (2007).

4 Kocabas, C. *et al.* Radio frequency analog electronics based on carbon nanotube transistors. *Proceedings of the National Academy of Sciences* **105**, 1405-1409 (2008).

5 Nougaret, L. *et al.* 80 GHz field-effect transistors produced using high purity semiconducting single-walled carbon nanotubes. *Applied Physics Letters* **94**, 243505-243503 (2009).

6 Wang, C. *et al.* Extremely Bendable, High-Performance Integrated Circuits Using Semiconducting Carbon Nanotube Networks for Digital, Analog, and Radio-Frequency Applications. *Nano Letters* **12**, 1527-1533 (2012).

7 Cao, Q. *et al.* Medium-scale carbon nanotube thin-film integrated circuits on flexible plastic substrates. *Nature* **454**, 495-500 (2008).

8 Sun, D.-m. *et al.* Flexible high-performance carbon nanotube integrated circuits. *Nat Nano* **6**, 156-161 (2011).

9 Snow, E. S., Perkins, F. K., Houser, E. J., Badescu, S. C. & Reinecke, T. L. Chemical Detection with a Single-Walled Carbon Nanotube Capacitor. *Science* **307**, 1942-1945 (2005).

10 Arnold, M. S., Green, A. A., Hulvat, J. F., Stupp, S. I. & Hersam, M. C. Sorting carbon nanotubes by electronic structure using density differentiation. *Nat Nano* **1**, 60-65 (2006).

11 Green, A. A. & Hersam, M. C. Nearly Single-Chirality Single-Walled Carbon Nanotubes Produced via Orthogonal Iterative Density Gradient Ultracentrifugation. *Advanced Materials* **23**, 2185-2190 (2011).

12 Zheng, M. & Semke, E. D. Enrichment of Single Chirality Carbon Nanotubes. *Journal of the American Chemical Society* **129**, 6084-6085 (2007).

13 Liu, H., Nishide, D., Tanaka, T. & Kataura, H. Large-scale single-chirality separation of single-wall carbon nanotubes by simple gel chromatography. *Nat Commun* **2**, 309 (2011).

14 Wu, J. *et al.* Short channel field-effect transistors from highly enriched semiconducting carbon nanotubes. *Nano Research* **5**, 388-394 (2012).

15 Krupke, R., Hennrich, F., Löhneysen, H. v. & Kappes, M. M. Separation of Metallic from Semiconducting Single-Walled Carbon Nanotubes. *Science* **301**, 344-347 (2003).

16 Tu, X., Manohar, S., Jagota, A. & Zheng, M. DNA sequence motifs for structure-specific recognition and separation of carbon nanotubes. *Nature* **460**, 250-253 (2009).

17 Li, X. *et al.* Langmuir−Blodgett Assembly of Densely Aligned Single-Walled Carbon Nanotubes from Bulk Materials. *Journal of the American Chemical Society* **129**, 4890-4891 (2007).

18 Engel, M. *et al.* Thin Film Nanotube Transistors Based on Self-Assembled, Aligned, Semiconducting Carbon Nanotube Arrays. *ACS Nano* **2**, 2445-2452 (2008).

19 LeMieux, M. C. *et al.* Self-Sorted, Aligned Nanotube Networks for Thin-Film Transistors. *Science* **321**, 101-104 (2008).

20 Wang, C., Ryu, K., Badmaev, A., Zhang, J. & Zhou, C. Metal Contact Engineering and Registration-Free Fabrication of Complementary Metal-Oxide Semiconductor Integrated Circuits Using Aligned Carbon Nanotubes. *ACS Nano* **5**, 1147-1153 (2011).

21 Patil, N. *et al.* Wafer-Scale Growth and Transfer of Aligned Single-Walled Carbon Nanotubes. *Nanotechnology, IEEE Transactions on* **8**, 498-504 (2009).

22 Zhou, W., Rutherglen, C. & Burke, P. Wafer scale synthesis of dense aligned arrays of single-walled carbon nanotubes. *Nano Research* **1**, 158-165 (2008).

23 Kocabas, C., Kang, S. J., Ozel, T., Shim, M. & Rogers, J. A. Improved Synthesis of Aligned Arrays of Single-Walled Carbon Nanotubes and Their Implementation in Thin Film Type Transistors†. *The Journal of Physical Chemistry C* **111**, 17879-17886 (2007).

24 Huang, H., Maruyama, R., Noda, K., Kajiura, H. & Kadono, K. Preferential Destruction of Metallic Single-Walled Carbon Nanotubes by Laser Irradiation. *The Journal of Physical Chemistry B* **110**, 7316-7320 (2006).

25 Collins, P. G., Arnold, M. S. & Avouris, P. Engineering Carbon Nanotubes and Nanotube Circuits Using Electrical Breakdown. *Science* **292**, 706-709 (2001).

26 Balasubramanian, K., Sordan, R., Burghard, M. & Kern, K. A Selective Electrochemical Approach to Carbon Nanotube Field-Effect Transistors. *Nano Letters* **4**, 827-830 (2004).

27 Banerjee, S. & Wong, S. S. Demonstration of Diameter-Selective Reactivity in the Sidewall Ozonation of SWNTs by Resonance Raman Spectroscopy. *Nano Letters* **4**, 1445-1450 (2004).

28 Hu, H. *et al.* Sidewall Functionalization of Single-Walled Carbon Nanotubes by Addition of Dichlorocarbene. *Journal of the American Chemical Society* **125**, 14893-14900 (2003).

29 Pop, E. The role of electrical and thermal contact resistance for Joule breakdown of single-wall carbon nanotubes. *Nanotechnology* **19**, 295202 (2008).

30 Javey, A. *et al.* High-Field Quasiballistic Transport in Short Carbon Nanotubes. *Physical Review Letters* **92**, 106804 (2004).

31 Xiao, J. *et al.* Alignment Controlled Growth of Single-Walled Carbon Nanotubes on Quartz Substrates. *Nano Letters* **9**, 4311-4319 (2009).

32 Ryu, K. *et al.* CMOS-Analogous Wafer-Scale Nanotube-on-Insulator Approach for Submicrometer Devices and Integrated Circuits Using Aligned Nanotubes. *Nano Letters* **9**, 189-197 (2008).

33 Liao, A., Zhao, Y. & Pop, E. Avalanche-Induced Current Enhancement in Semiconducting Carbon Nanotubes. *Physical Review Letters* **101**, 256804 (2008).

34 Liao, A. *et al.* Thermal dissipation and variability in electrical breakdown of carbon nanotube devices. *Physical Review B* **82**, 205406 (2010).

35 Dai, J. *et al.* Molecular Glass Resists for High-Resolution Patterning. *Chemistry of Materials* **18**, 3404-3411 (2006).

36 Islam, A. E. *et al.* Effect of variations in diameter and density on the statistics of aligned array carbon-nanotube field effect transistors. *Journal of Applied Physics* **111**, 054511-054517 (2012).

37 Varesi, J. & Majumdar, A. Scanning Joule expansion microscopy at nanometer scales. *Applied Physics Letters* **72**, 37-39 (1998).

38 Wulf, M., Michel, S., Jenschke, W., Uhlmann, P. & Grundke, K. A new method for the simultaneous determination of surface tension and density of polymer melts. *Physical Chemistry Chemical Physics* **1**, 3899-3903 (1999).

39 Jin, S. H. *et al.* Sources of Hysteresis in Carbon Nanotube Field-Effect Transistors and Their Elimination Via Methylsiloxane Encapsulants and Optimized Growth Procedures. *Advanced Functional Materials* **22**, 2276-2284 (2012).

40 Jin, S. H. *et al.* Pentacene OTFTs with PVA Gate Insulators on a Flexible Substrate. *Journal of the Korean Physical Society* **44**, 181 (2004).

2.8 Figures

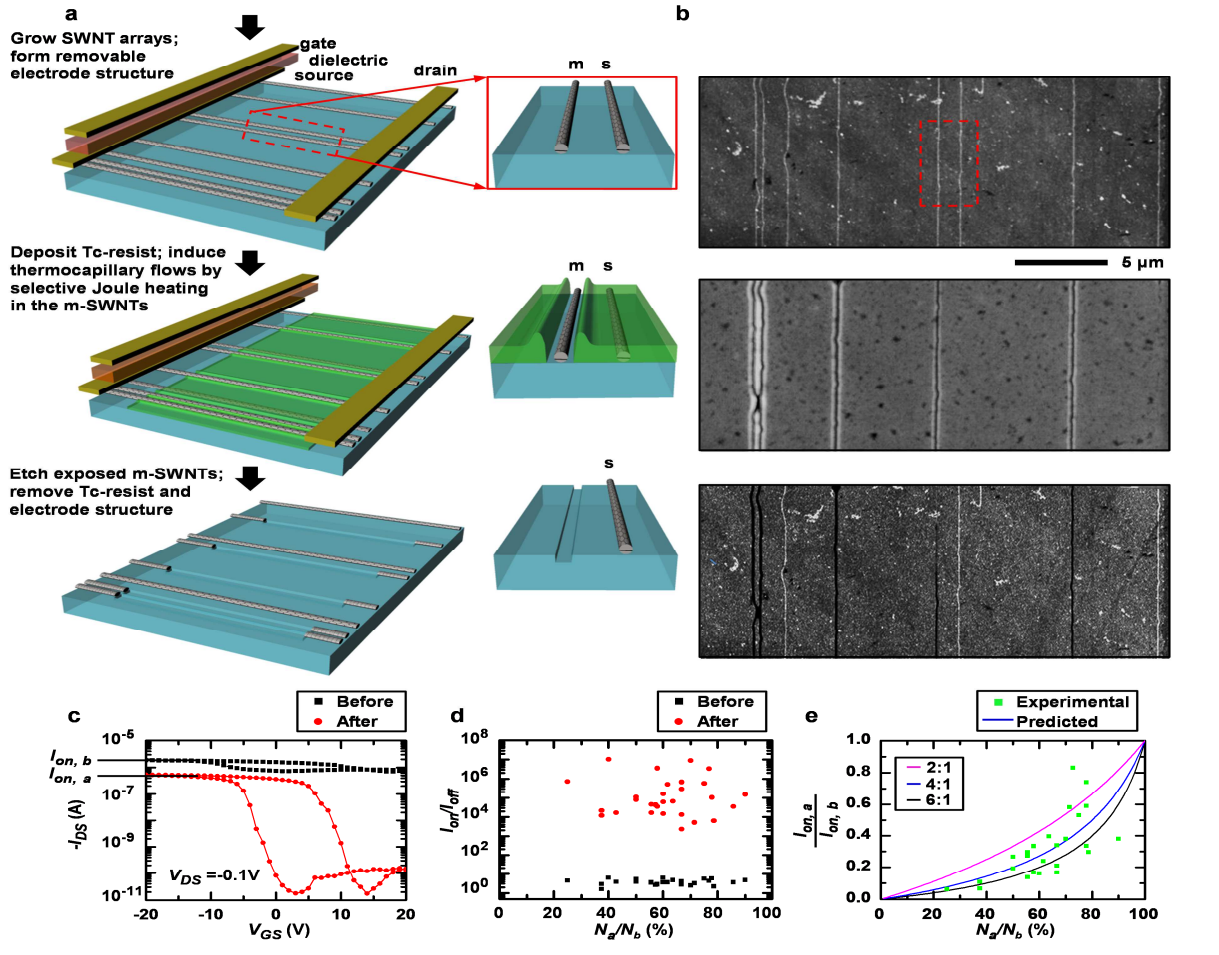

Figure 2.1 Process for exploiting thermocapillary effects in the purification of arrays of SWNTs. (a,b) Schematic illustration and corresponding AFM images of various stages of the process, which we refer to as thermocapillary-enabled purification (TcEP), as applied to an array of SWNTs that consists of five m-SWNTs and three s-SWNTs. Uniform thermal evaporation forms a thin, amorphous organic layer that functions as a thermocapillary resist (Tc-resist). A series of processing steps defines a collection of electrodes and dielectric layers for selective injection of current into the m-SWNTs. The Joule heating that results from this process induces thermal gradients that drive material flow in the Tc-resist away from the m-SWNT, to form open trenches with widths, measured near the substrate, of ~100 nm. Reactive ion etching physically eliminates the m-SWNT exposed in this fashion, while leaving the coated s-SWNTs unaltered. Removing the Tc-resist and electrode structures completes the process, to yield arrays comprised only of s-SWNTs. (c) Typical transfer characteristics for a transistor built with an array of SWNTs in a partial gate geometry, evaluated before and after TcEP. The quantities $I_{on,b}$ and $I_{on,a}$ correspond to currents measured in the on states before and after TcEP, respectively. Here, the on/off ratio improves by 2×10^4 times, while $I_{on,a}$ / $I_{on,b}$ remains relatively large, i.e. ~0.25. (d) Ratios between currents in the on and off states before and after TcEP ($I_{on,b}$ and $I_{off,a}$ respectively) as a function of the ratio of the difference between number of SWNTs before and after TcEP (N_b and N_a, respectively) to the N_b. All devices show on/off ratios > $2x10^3$, with most > $1x10^4$. This result is consistent with complete removal of all m-SWNT. (e) Ratio of $I_{on,a}$ to $I_{on,b}$ as a function of (N_b-N_a) / N_b , for the entire set of devices with $N_b > 7$. The results are consistent with modeling (lines) that assumes 100% retention of s-SWNTs through the TcEP process, expected relative populations of s-SWNTs and m-SWNTs in the arrays, and ratios of conductivities of m-SWNTs and s-SWNTs (in the their on state) that lie between experimentally expected values.

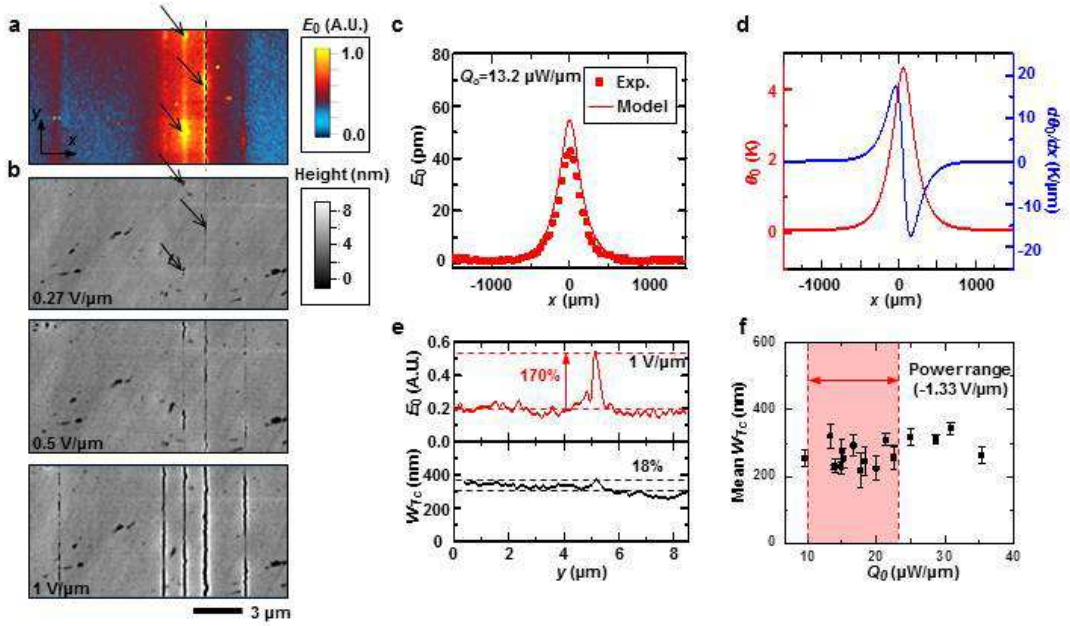

Figure 2.2 Thermal origins and power scaling in operation of Tc-resists. (a) SJEM image of an array of SWNTs in an operating, two-terminal device on quartz. The electrodes (separation ~30 μm) are above and below the image, out of the field of view. The coordinates *x* and *y* lie perpendicular and parallel, respectively, to the direction of alignment of the SWNTs. (b) AFM topographical images of the same device shown in the SJEM image of (a), coated with a thin (~25 nm) layer of Tc-resist, collected after operation at bias conditions of 0.27 (top), 0.5 (middle) and 1.0 V / μm (bottom). Comparison of these images to those collected by SJEM reveals a clear correlation between AC expansion (E_0; and, therefore, temperature) and formation of trenches in the Tc-resist (DC heating). (c) AC Thermal expansion, E_0, induced by Joule heating in an individual SWNT with input power density Q_0 ~ 13 μW / μm (peak to peak) measured by SJEM (line) as a function of position *x*, where *x*=0 is the location of the SWNT, on a SiO_2/Si substrate and results of thermomechanical modeling (symbols), illustrating excellent agreement in both magnitude and shape. (d) Computed AC temperature rise, θ_0, and thermal gradients ($d\theta_0/dx$) at the surface of the Tc-resist using experimentally validated models, for the case of the SWNT in (c). The results indicate small increases in temperature for levels of Joule heating that induce trenches in the Tc-resist (~3-10 μW / μm). (e) The top graph shows AC thermal expansion (arbitrary units) measured by SJEM along the length (*y*) of the fourth SWNT from the left in the array that appears in (a) and (b). The bottom graph shows the width of the corresponding trench that appears in the Tc-resist (W_{Tc} measured at the top of the film) for an applied bias of ~1 V / μm. The results show variations in W_{Tc} that are nearly ten times smaller than those in expansion (and therefore temperature). (f) Measurements of the average W_{Tc} as a function of Q_0. The results show no systematic dependence on Q_0 over this range. The highlighted region corresponds to the values of Q_0 associated with optimized conditions for TcEP.

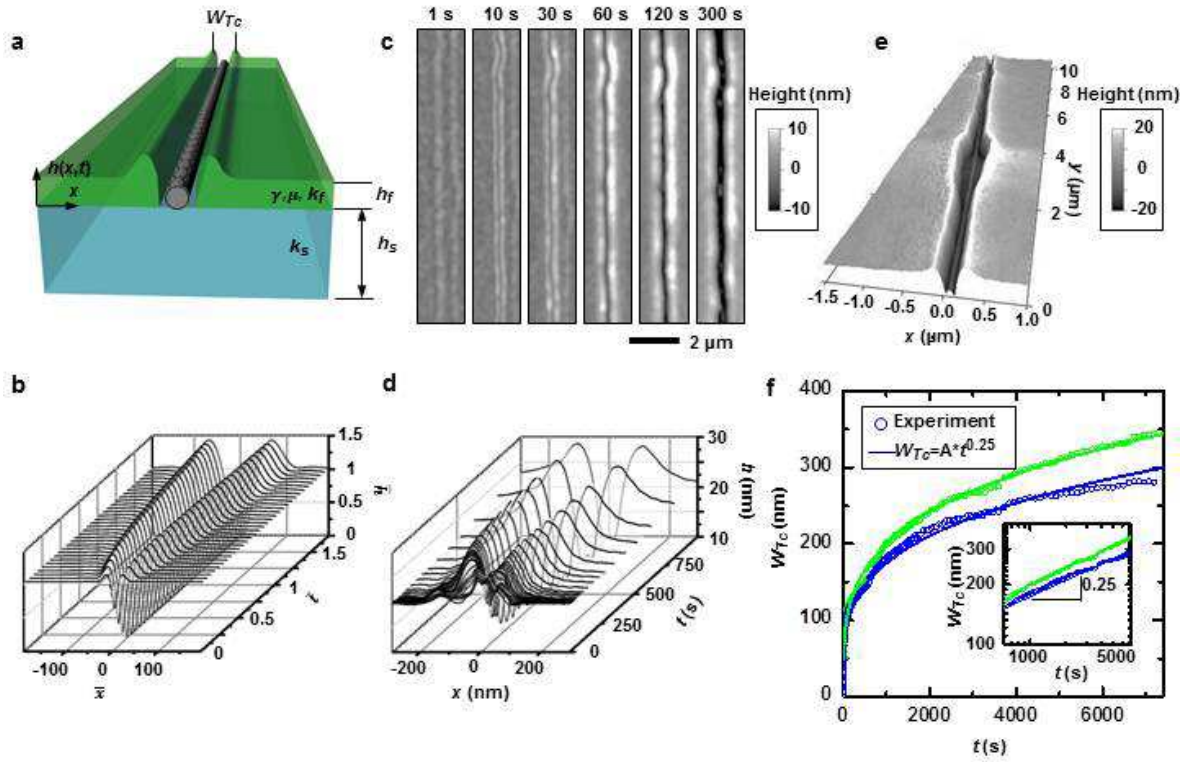

Figure 2.3 Nanoscale thermocapillary flows in Tc-resists induced by Joule heating in SWNTs. (a) Schematic illustration of the geometry of the system, with key parameters defined. The SWNT, the Tc-resist and the substrate are grey, green and blue, respectively. (b) Theoretically calculated normalized surface profiles of the Tc-resist ($\bar{h}$), as a function of normalized distance ($\bar{x}$) and time ($\bar{t}$), showing the evolution of the trench geometry with thermocapillary flow. (c) AFM images of a SWNT coated with Tc-resist (~25 nm), at times for Joule heating (0.66 V/μm) of 1, 10, 30, 60, 120 and 300 s, induced by current injection at electrodes that lie outside of the field of view. Thermocapillary flow creates a trench that aligns to the SWNT and grows in width over time. (d) Averaged cross sectional profiles extracted from measurements like those shown in (c). The results compare favorably to the modeling in (b). (e) AFM image, rendered in a 3D perspective view collected at a duration of 1800 s. The width in this case is sufficiently large that AFM measurements reveal clearly that thermocapillary flow completely and cleanly exposes the SWNT at the base of the Tc-resist. (g) Widths of trenches measured by AFM from the ridges that form at the top surface (W_{Tc}) as a function of time of Joule heating in two different SWNTs, at a field of 0.66V/μm. Both model and experiment show a power law time dependence with an exponent of 0.25.

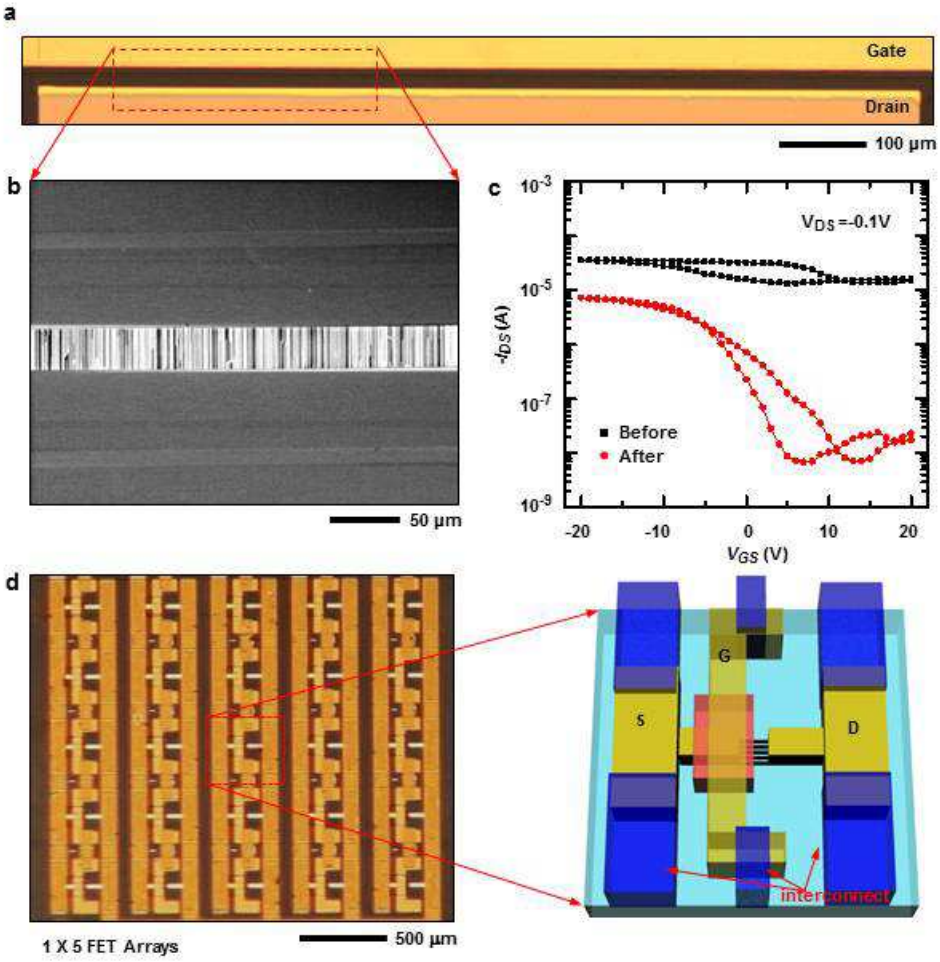

Figure 2.4 Two approaches to scaled implementation of TcEP. (a) Optical microscope image of a set of electrodes for TcEP on a large-scale array of SWNTs, which in this example allows purification of ~500 SWNTs. (b) Scanning electron microscope image of a small region of the structure shown in (a). (c) Transfer characteristics before and after removal of m-SWNTs by TcEP from the region between the electrodes shown in (a). The results indicate outcomes consistent with observations of small-scale implementations of TcEP, i.e. high on/off ratios ~1×10^3 and modest reductions in on current ($I_{on,\,a}$ / $I_{on,\,b}$ ~20%). (d) Optical micrograph and schematic illustration of alternative mode for scaled implementation of TcEP. Here, an interconnected array of 25 sets of electrodes allows TcEP over a collection of small regions, in a parallel fashion. Associated transfer curves are similar to those shown in (c).

CHAPTER 3: DETAILS OF THERMOCAPILLARY-ENHANCED PURIFICATION

3.1 Individual SWNT Thermocapillary Trench Experiments

Thermocapillary flows in Tc-resists were studied (5 min, 60 ˚C background heating) using devices that incorporate single or several SWNTs. Devices were fabricated in geometries to ensure that only 1 or 2 SWNTs were present in the channel, as confirmed by AFM. In the case of single SWNT devices, the electronic type could be determined directly from the electrical properties (on/off ratio > 100, s-SWNT; on/off ratio < 10, m-SWNT). For devices with 2 SWNTs that exhibited high on/off ratio, both SWNTs must be s-SWNTs. For similar devices with low on/off ratio before TcEP and high on/off ratio after TcEP, one SWNT must be an m-SWNT and the other an s-SWNT. Devices with two m-SWNTs were not used for these experiments. Biases were applied to increase the resistance of the s-SWNTs (i.e. their "off" state, at +20 V_{GS}), resulting in relatively low (high) current levels for all s-SWNTs (m-SWNTs). As a result, all 2-SWNT devices fell into one of two cases: their currents were dominated by a single m-SWNT or they contained two s-SWNTs. For the second case, one s-SWNT is likely to dominate, but at worst, the s-SWNT have roughly equal current levels in which case the data served as an upper limit for the actual current and could be as little as half that level. The large number of devices that were studied and the observation that most s-SWNTs showed current levels more than ten times below the threshold for trench formation suggest that assumptions concerning relative current distributions in s-SWNTs are unlikely to affect the broad conclusions. The thresholds were accurately defined by devices with just one SWNT. We performed systematic studies of trenches formed under a range of input powers for single s-SWNTs and single m-SWNTs. A range of outcomes for input powers of 0.1-30 μW/μm (SWNT length = 30 μm) were observed by AFM (Fig. 3.1a). For all experiments, powers below 3.3 μW/μm led to no

trenches. For powers of 3.3-10 μW/μm most devices exhibited trenches, but only partly along the lengths of the SWNTs. For all experiments with powers greater than 10 μW/μm, trenches with widths W_{Tc}~250-300 nm, were observed along the entire lengths of the SWNTs. This analysis provides information on threshold powers for trench formation, which, via analytical modeling, can be correlated to peak temperatures of ~2-5 ˚C. By sorting these same results by input field and SWNT electronic type (Fig. 3.1b), optimized conditions can be established. At fields below the optimal range, the heating is insufficient to yield trenches along the entire lengths of all of the m-SWNTs; at higher fields, the most conductive s-SWNTs begin to show partial trench formation. However, for optimized conditions, all s-SWNTs yielded no trenches, while all m-SWNTs yield complete trenches, as required for proper operation of TcEP.

3.2 Deposition Conditions for the Tc-resist and its Properties

Figure 3.2a shows the chemical structure of the Tc-resist. The material was deposited via thermal evaporation. Figure 3.2b shows AFM images of a film deposited on a SiO_2/Si substrate. The surface roughness is comparable to that of the underlying substrate, i.e. 2-3 Å. Experiments that involved heated substrates (quartz or SiO_2/Si) with thin coatings of Tc-resist (~25 nm thickness) showed an onset of dewetting between 80-120 ˚C, depending on substrate hydrophobicity. Clean, hydrophilic surfaces yielded higher dewetting temperatures. In vacuum (~$1x10^{-4}$ torr), sublimation began at ~100 ˚C, as determined by experiments using lithographically patterned, calibrated resistive heaters of Pt (lengths ~1-3 mm, widths ~6-10 μm). Differential scanning calorimetry (dry nitrogen) yielded a specific heat of ~1.5 J/C/cm^3 (Fig. 3.2c, T_m= 225 ˚C, T_g= 95 ˚C, T_{rc}=155 ˚C). Time-resolved, picosecond pump-probe experiments based on thermoreflectance[1] using relatively thick films (300 nm, Fig 3.2d) yielded thermal conductivities of ~0.2 W/m/K, similar to most organic thin films.

3.3 Single SWNT Conductance Statistics

The large number of SWNTs studied by TcEP on devices with small arrays of SWNTs provided statistics on the process. For each array, the number of SWNTs and the values of $I_{on,\,b}$ and $I_{on,\,a}$ (shown for a typical device, Fig 3.3b) together with an assumption that all of the removed SWNTs are m-SWNTs and all of the remaining SWNTs are s-SWNTs, yields estimates for the average conductance of these two types of SWNTs, for each device. Figure 3.3a shows a histogram of the conductances of individual SWNTs determined in this way. (We note that a device with 3 s-SWNTs and an average conductance of 50 kΩ/μm is counted 3 times.) The mean conductances for m-SWNTs and s-SWNTs (in their on state) are 17 kΩ/μm and 75 kΩ/μm, respectively. These distributions are in the range of those reported for single SWNTs studied previously[2]; with values of 35 kΩ/μm (m-SWNTs) and 55 kΩ/μm (s-SWNTs) for backgated devices (Fig. 3.3c)[2]; and 140 kΩ/μm (m-SWNTs) and 1000 kΩ/μm (s-SWNTs) for top gated devices.[2] Using the experimentally observed ratios of numbers of m-SWNTs to s-SWNTs, and a ratio of mean conductances of ~4:1, the assumption that TcEP preserves all s-SWNT is consistent with observations.

3.4 Partial Gate Device Properties

The electrode geometries used for TcEP involved a partial gate structure shown schematically in Fig. 2.1a. This configuration results in reduced gate-drain fields, which minimize Schottky barrier tunneling, band-to-band tunneling and avalanche phenomena.[3] The operation avoids ambipolar conduction at the bias conditions needed for TcEP (characterization at conditions consistent with TcEP, 60 ˚C background heating, ~$1x10^4$ torr). These effects are clearly observed in transfer characteristics for devices based on an individual s-SWNT in partial gate (Fig. 3.4a) and full gate (Fig. 3.4b) layouts. Here, the same SWNT, same pair of source-

drain electrodes, and dielectric were used for both devices. The only difference is the length of gate extension into the channel. Both configurations exhibit ideal device behavior at low bias (V_{DS}=-0.1 V). At high bias (V_{DS}<-10 V, L=30 μm), however, the full gate device shows pronounced ambipolar conduction, unlike the partial gate case. Figure 3.3c illustrates the effect of source-drain bias and gate overlap (L_{ov}) on on/off ratio, where all measurements were performed on the same SWNT. The device with 5 μm gate overlap (i.e. the configuration used for TcEP) exhibits on/off ratios 2-3 orders of magnitude higher than the device with full overlap (L_{ov}=30 μm). Figure 3.4d shows the ability of the partial gate configuration to maintain current levels several orders of magnitude lower than that of the full gate configuration, even for long bias durations ("off" state, V_{DS}=-40V, V_{GS}=+20V, 5 min, consistent with TcEP experiments).

3.5 SJEM Experiments

Figure 3.5a shows an SJEM image of an array of SWNTs (two-terminal device, SiO_2 (200 nm) / Si substrate) covered with a 120 nm thick film of PMMA, collected at the condition of $V(t) = V_{DS}\cos(2\pi ft)$ with V_{DS}=3V and f=30kHz and V_{GS}=0V. Figure 3.5a shows the integrated expansion percentage (I.E.P.). To determine this quantity, we first located the maximum expansion along each measured cross-section perpendicular to the length of the SWNT. Next, we integrated these values along each SWNT, to get the integrated expansion (I.E.). The I.E.P. is the ratio of the I.E. to the sum of the I.E. for all three SWNTs, times 100%. Since the maximum expansion is proportional to the input power, the I.E.P. can be used to estimate the power input for each SWNT, from the measured total power into the device. Figure 3.5c shows a 3D rendering of the SJEM signal for the SWNT associated with Fig. 2.2b. Figure 3.5d shows a schematic of the SJEM measurement.

3.6 Computed Temperature Distributions Associated with Joule Heating in Individual SWNTs

In this section, we describe procedures for determining the temperature distribution resulting from a SWNT embedded in a film of PMMA on SiO_2/Si substrate with power dissipation at the SWNT for an AC applied voltage. The temperature rise at the surface of the Tc-resist can be obtained by considering first the analytical solution for a disk heat source with radius r_0 at the interface between the Tc-resist and the SiO_2. Here, a cylindrical coordinate system is set such that the origin is coincident with the center of the heat source as shown in Fig. 3.6a,b. The heat transfer governing equation temperature in cylindrical coordinate is

$$\frac{\partial^2 T}{\partial r^2}+\frac{1}{r}\frac{\partial T}{\partial r}+\frac{\partial^2 T}{\partial z^2}-\alpha\frac{\partial T}{\partial t}=0 \tag{1}$$

where $\alpha=\dfrac{k}{c\rho}$ is thermal diffusivity, k is thermal conductivity, ρ is density, and c is specific heat capacity. The subscripts 0, 1 and 2 denote Tc-resist, SiO_2 and Si, respectively. Setting $\theta=T-T_\infty$, where T_∞ is the remote temperature, the above equation is equivalent to

$$\frac{\partial^2 \theta}{\partial r^2}+\frac{1}{r}\frac{\partial \theta}{\partial r}+\frac{\partial^2 \theta}{\partial z^2}=\alpha\frac{\partial \theta}{\partial t} \tag{2}$$

The boundary conditions are

(1) $z=-h_0$ (top surface)

$$-k_0\left.\frac{\partial \theta}{\partial z}\right|_{z=-h_0}=0 \tag{3}$$

(2) $z=0$

$$\theta_{0^+} = \theta_{0^-},\ -k_0 \left.\frac{\partial \theta}{\partial z}\right|_{z=0^-} = \begin{cases} Q_1 & 0 \le r \le r_0 \\ Q_{c1} & r_0 < r < +\infty \end{cases},\ -k_1 \left.\frac{\partial \theta}{\partial z}\right|_{z=0^+} = \begin{cases} Q_2 & 0 \le r \le r_0 \\ Q_{c1} & r_0 < r < +\infty \end{cases} \tag{4}$$

where Q_1 and Q_2 satisfy $-Q_1 + Q_2 = \dfrac{P}{\pi r_0^2}$, P is the total power of the disk.

(3) $z = h_1$

$$\theta_{h_1^+} = \theta_{h_1^-} \text{ and } -k_1 \left.\frac{\partial \theta}{\partial z}\right|_{z=h_1} = -k_2 \left.\frac{\partial \theta}{\partial z}\right|_{z=h_1} \tag{5}$$

(4) $z = h_1 + h_2 \sim \infty$

$$\theta_{h_1+h_2} = 0 \tag{6}$$

For a voltage $V(t) = V_0 \cos(\omega t)$ with angular frequency $\omega = 2\pi f$, the Joule heating has angular frequency 2ω. The total power of the disk can then be obtained as $P(t) = P_0 \left[1 + \cos(2\omega t)\right]/2$, which yields a constant temperature rise (DC component) due to $P_0/2$ and a time oscillating temperature rise (AC component) due to $P_0 \cos(2\omega t)/2$. It should be noted that the DC component of temperature rise can be easily obtained by setting ω=0 in the solution of AC component.

The time oscillating temperature rise (AC component) has the same frequency as the power density, i.e. $\theta(r, z, t) = \theta(r, z)\exp(2\omega t i)$. Therefore, we have

$$\frac{\partial^2 \theta}{\partial r^2} + \frac{1}{r}\frac{\partial \theta}{\partial r} + \frac{\partial^2 \theta}{\partial z^2} - q^2 \theta = 0 \tag{7}$$

where $q^2 = \dfrac{2\omega i}{\alpha}$ and $\theta = \theta(r, z)$.

Equation (7) can be solved via the Hankel transform, for which the following transform pair of the first kind is applicable:

$$\begin{aligned}\varphi(r,z) &= \int_0^\infty \bar{\varphi}(\xi,z)\, J_0(\xi r)\,\xi \mathrm{d}\xi \\ \bar{\varphi}(\xi,z) &= \int_0^\infty \varphi(r,z)\, J_0(\xi r)\, r\mathrm{d}r\end{aligned} \tag{8}$$

where $\varphi(r,z)$ is the original function, $\bar{\varphi}(\xi,z)$ is the transform, and J_0 is the 0^{th} order Bessel function of the first kind. Equation (7) then becomes

$$\frac{d^2\bar{\theta}}{dz^2} - (\xi^2 + q^2)\bar{\theta} = 0 \tag{9}$$

Solving the above equation gives

$$\bar{\theta} = A\exp(z\sqrt{\xi^2+q^2}) + B\exp(-z\sqrt{\xi^2+q^2}) \tag{10}$$

where A and B are two unknown functions to be determined according to boundary and continuity conditions. The temperature rise is then obtained by

$$\theta = \int_0^\infty \left(A\mathrm{e}^{-\xi z} + B\mathrm{e}^{\xi z}\right) J_0(\xi r)\,\xi \mathrm{d}\xi \tag{11}$$

Therefore, the temperature rise in Hankel space at each layer is obtained as

Tc-resist: $\bar{\theta}_0(\xi,z) = A_0\exp(z\sqrt{\xi^2+q_0^2}) + B_0\exp(-z\sqrt{\xi^2+q_0^2})$

SiO2 layer: $\bar{\theta}_1(\xi,z) = A_1\exp(z\sqrt{\xi^2+q_1^2}) + B_1\exp(-z\sqrt{\xi^2+q_1^2})$

Si layer: $\bar{\theta}_2(\xi,z) = A_2\exp(z\sqrt{\xi^2+q_2^2}) + B_2\exp(-z\sqrt{\xi^2+q_2^2})$

With BCs (3)-(6) in Hankel space, we can obtain the temperature at each layer. For example, A_0 and B_0 are given by

$$A_0 = \frac{\kappa+1}{(1-\kappa)\left[1+\exp(-2h_0\sqrt{\xi^2+q_0^2})\right]+(\kappa+1)\dfrac{k_0\sqrt{\xi^2+q_0^2}}{k_1\sqrt{\xi^2+q_1^2}}\left[1-\exp(-2h_0\sqrt{\xi^2+q_0^2})\right]} \frac{P_0}{k_1\pi\xi\sqrt{\xi^2+q_1^2}} \frac{J_1(\xi r_0)}{2r_0} \tag{12}$$

$$B_0 = A_0\exp(-2h_0\sqrt{\xi^2+q_0^2})$$

where

$$\kappa = \frac{1-\dfrac{k_2}{k_1}\dfrac{\sqrt{\xi^2+q_2^2}}{\sqrt{\xi^2+q_1^2}}}{1+\dfrac{k_2}{k_1}\dfrac{\sqrt{\xi^2+q_2^2}}{\sqrt{\xi^2+q_1^2}}}\exp(-2h_1\sqrt{\xi^2+q_1^2})$$

The temperature rise due to the disk heat source can be obtained by Eq. (11). For example, the temperature rise in the Tc-resist is obtained as

$$\theta(r,z) = \int_0^{+\infty} A_0\left[\exp(z\sqrt{\xi^2+q_0^2})+\exp(-z\sqrt{\xi^2+q_0^2}-2h_0\sqrt{\xi^2+q_0^2})\right]\cdot J_0(\xi r)\,\xi d\xi \tag{13}$$

The surface temperature rise of the Tc-resist is then obtained by setting $z=-h_0$ as

$$\theta(r) = \int_0^{+\infty} 2A_0\exp(-h_0\sqrt{\xi^2+q_0^2})\cdot J_0(\xi r)\,\xi d\xi \tag{14}$$

As $r_0 \to 0$, we obtain the temperature rise due to a point heat source as

$$\theta_P(r) = \frac{1}{4k_1\pi}\int_0^{+\infty} \frac{(\kappa+1)J_0(\xi r)\,\xi}{(1-\kappa)\cosh(h_0\sqrt{\xi^2+q_0^2})+(\kappa+1)\dfrac{k_0\sqrt{\xi^2+q_0^2}}{k_1\sqrt{\xi^2+q_1^2}}\sinh(h_0\sqrt{\xi^2+q_0^2})}\cdot\frac{P_0}{\sqrt{\xi^2+q_1^2}}d\xi \tag{15}$$

For a point heat source at $(0,\eta,0)$ with heat generation $P_0 = Q_0 \cdot d\eta$ and Q_0 as the power density, the integration of Eq. (15) with $r = \sqrt{(\eta - y)^2 + x^2}$ gives the temperature rise at point (x, y) due to a line heat source as

$$\theta(x,y) = \frac{1}{4k_1\pi}\int_{-L/2}^{L/2} d\eta \int_0^{+\infty} \frac{(\kappa+1)J_0\left(\xi\sqrt{(\eta-y)^2+x^2}\right)\xi}{(1-\kappa)\cosh(h_0\sqrt{\xi^2+q_0^2}) + (\kappa+1)\dfrac{k_0\sqrt{\xi^2+q_0^2}}{k_1\sqrt{\xi^2+q_1^2}}\sinh(h_0\sqrt{\xi^2+q_0^2})} \cdot \frac{Q_0}{\sqrt{\xi^2+q_1^2}} d\xi \qquad (16)$$

It should be noted that Eq. (16) gives the magnitude of time oscillating temperature rise, i.e., θ_0 in the main text is equal to $2\theta(x,y)$. The total surface temperature rise can be obtained as $\theta(x,y,t) = \theta(x,y)\big|_{\omega=0} + \theta(x,y)\cos(4\pi ft) = \left[\theta_1 + \theta_0\cos(4\pi ft)\right]/2$ due to a line heat source with power density $Q(t) = Q_0\left[1+\cos(2\omega t)\right]/2$.

Under the assumptions of (1) plane strain in y direction since the length of SWNT (~30μm) is much larger than its radius and (2) plane stress in z direction since the film is very thin (~25nm), the peak-peak value of AC surface thermal expansion (i.e., the out-of-plane displacement) of the Tc-resist can be obtained as

$$E_0 = \frac{1+\nu_0}{1-\nu_0}\beta_0 h_0 \theta(x, y=-h_0) \qquad (17)$$

where ν_0 and β_0 are the Poisson's ratio and coefficient of thermal expansion of the PMMA, respectively.

Setting $k_2 = k_1 = k_s$, $k_0 = k_f$, $h_0 = h_f$ and ω=0, Eq. (16) gives the surface temperature of Tc-resist for Tc-resist/quartz under DC voltage as

$$\theta(x,y)=\frac{1}{2k_s\pi}\int_{-L/2}^{L/2}d\eta\int_0^{\infty}\frac{Q_0J_0\left(\xi\sqrt{(\eta-y)^2+x^2}\right)}{\cosh(\xi h_f)+\frac{k_f}{k_s}\sinh(\xi h_f)}\mathrm{d}\xi \tag{18}$$

where k_f and k_s are the thermal conductivity of Tc-resist and quartz, respectively, and h_f is the thickness of Tc-resist

A 3D finite element model was established to study the temperature distribution in the system and validate the analytical model. Eight-node, hexahedral brick elements in the finite element software ABAQUS are used to discretize the geometry. A volume heat source was applied on the SWNT. The zero heat flux boundary was applied at the top surface of the Tc-resist, and a constant temperature T_∞ is applied at the bottom of the quartz substrate. The finite element simulations agree well with analytical modeling as shown in Fig. 3.6c for the surface temperature of the Tc-resist k_0 = 0.2W/m/K, k_f = 6W/m/K, $Q_0 = 16.7\mu$W/μm and L=30μm.

3.7 Modeling of Thermocapillary Flow in TcEP

The viscous flow of Tc-resist is essentially unidirectional and the evolution of film thickness $h(x,t)$ can be obtained from a lubrication equation

$$\frac{\partial h}{\partial t}+\frac{\partial}{\partial x}\left[\frac{\tau h^2}{2\mu}+\frac{h^3}{3\mu}\frac{\partial}{\partial x}\left(\gamma\frac{\partial^2 h}{\partial x^2}\right)\right]=0 \tag{19}$$

where γ is the surface tension, which usually linearly depends on the temperature rise (i.e., $\gamma=\gamma_0-\gamma_1\theta$), $\tau=\frac{\partial\gamma}{\partial T}\frac{\partial T}{\partial x}$ is the thermocapillary stress with $T=T_\infty+\theta$, and μ is viscosity. By introducing the non-dimensional terms $\bar{h}=h/h_f$, $\bar{x}=x/h_f$, $\bar{t}=\gamma_1Q_0t/\left(\mu_0k_fh_f^2\right)$, $\bar{\mu}=\mu/\mu_0$,

$\bar{\gamma} = k_f h_f \gamma / (Q_0 \gamma_1)$, $\bar{\tau} = \partial\bar{\theta}/\partial\bar{x}$ and $\bar{\theta} = k_f h_f \theta / Q_0$, Equation (19) can be written in non-dimensional form as

$$\frac{\partial \bar{h}}{\partial \bar{t}} + \frac{\partial}{\partial \bar{x}}\left[\frac{\bar{\tau}\bar{h}^2}{2\bar{\mu}} + \frac{\bar{h}^3}{3\bar{\mu}}\frac{\partial}{\partial \bar{x}}\left(\bar{\gamma}\frac{\partial^2 \bar{h}}{\partial \bar{x}^2}\right)\right] = 0 \qquad (20)$$

The Fortran solver PDE_1D_MG can be used to solve for $\bar{h}$.

3.8 Experimental and Theoretical Time Dependence of Trench Evolution in TcEP

The time dependence of trench evolution was studied for a small area (3×3 μm) within an array of SWNTs by collecting a sequence of AFM images (~30 s), for different durations of applied bias (V_{DS}=0.66 V/μm, L= 30 μm, 30 ˚C background heating) . During imaging no bias was applied, thereby leaving the trenches in fixed geometries for the duration of the measurement. In between images, biases were applied, driving trench formation for controlled durations (durations varied depending on accumulated duration ranging from 0.1 s for very short accumulated duration, <10 s, to 30 min for very long accumulated duration, 6-8 hrs). The total time of trench formation was taken to be the sum of the durations for all preceding experiments. Figure 3.7 shows representative images at various points in the evolution of trenches (Fig. 2.3c shows cropped images associated with the second trench from the left). At relatively short durations, trenches were shallow (< 1 nm deep) and characterized by slight ridges in the Tc-resist on each side of the SWNT, over time evolving into fully formed trenches, which grew and eventually (hours) began to interact with trenches from adjacent SWNTs, limiting further growth. Data associated with analysis of time dependence was restricted to durations where trenches were isolated from one another (<2 hr). For the purposes of establishing reliable measures of trench evolution, the trench width, W_{Tc}, was defined as the width between the peak of the pile-up

on either side of the trench (actual minimum widths, evaluated at the base of the Tc-resist, were much narrower). Analysis to determine the left and right side of the trench was performed in MATLAB, and involved identifying the first location to the left and right side of the trench where the slope fell below a certain threshold, $5x10^{-11}$. Figure 3.8a shows an AFM image for t=600 s with the identified left and right sides of the trench highlighted for the three central trenches. Figure 3.8b shows cross-sectional profiles associated with the central trench at various points in the trench evolution and the identified left and right positions. Figures 2.3f and 3.9a show the resulting experimentally extracted W_{Tc}. Smaller trenches (W_{Tc}<150 nm, associated with t<10 min), were less distinct, and identifying the left and right positions was more difficult. While values of W_{Tc} were roughly accurate, there was significantly more error at shorter times than longer times. The short time values were not used for power law fitting (Fig 3.9a). Power law fitting was performed in data ranges where the standard deviation was <10% of W_{Tc} (for data outside of this range, standard deviation was W_{Tc} ~20-50% of W_{Tc}). The data fit well to a power law with exponent 0.25 (the values are for the constant of proportionality, A, are shown). Figure 3.9b shows the predicted W_{Tc} based on modeled trench profiles (peaks in $\bar{h}(\bar{x},\bar{t})$), which also fit well to a power law with exponent of 0.25 (the parameter A depends on various Tc-resist properties, several of which are unknown). Figures 3.9c,d show the predicted W_{Tc} for power densities varying from 8.3-33.3 μW/μm for long durations and for durations that yield trench widths associated with those typical for TcEP. (Comparison to model can be difficult given the uncertainty in material properties for the Tc-resist. Because $\bar{t}$ is normalized with respect to μ and γ, which are unknown, it is not possible to compare directly to t. Nevertheless, the computed W_{Tc} is only normalized by h_0, so it is meaningful to compare modeled $\bar{t}$ to ranges of experimental t that yield trenches of similar size to those measured experimentally.) For long times, W_{Tc} varies

with power density. At durations associated with experimental conditions, however, almost no variation is predicted. This relative insensitivity to power is consistent with experimental observation (Fig. 2.2e,f), where only~20% variations in W_{Tc} are typically observed. Such variations likely result from local changes in film viscosity associated with heating, or other effects not explicitly included in the model.

3.9 Thermocapillary Flows in Tc-resist, Studied by Heated AFM Tips with Integrated Temperature Sensors

Heated atomic force microscope (AFM) tips with known temperatures contacted with the Tc-resist layer for various times, and with various applied powers, allow study of the effects of thermocapillary flow in a nanoscale system where temperature and other parameters are controlled (and known) more accurately than the case for SWNTs. The heated tip (radius <100 nm) was fabricated from doped single crystal silicon, and is capable of reaching temperatures of 1000 °C with a temperature calibration to within 5 °C for this entire range.[4] Previous studies of viscous mass flow from a heated tip to a substrate revealed thermocapillarity to be an important driver of flow.[5] Figure 3.10 shows Tc-resist layer deformation induced by tip heating for tip-substrate temperature differences between 5 and 45 °C and dwell times between 0.1 and 300 s on both an unheated Tc-resist layer and a Tc-resist layer heated to 50 °C. The tip dwelled on the surface with tip forces below 20 nN and did not deform the surface when unheated. The results show that significant material flows radially away from the heated tip for Tc-resist layer temperatures far below the sublimation temperature, consistent with thermocapillary stresses induced by the temperature gradient around the tip.

3.10 Pulsed Heating in TcEP for Large Scale Arrays of SWNTs

For arrays that contain large numbers of SWNTs (either at high densities or over large areas) the coupled heating of many SWNT leads to bulk, and sometimes large, increases in temperature. These effects can yield thermocapillary flow on larger length scales and in ways that are difficult to confine to the positions of the SWNTs (Fig. 3.11). Pulsed bias conditions (~1-10 μs) can avoid these cumulative effects, to yield localized heating and thereby preserve well-behaved trenches even with large arrays of SWNTs and/or relatively high densities (up to 3 SWNT/μm studied here). Figure 3.11, shows the resulting trenches for a localized region within a large area high density array (30 μm x 1 mm, 2-3 SWNT/μm) for increasing duty cycles (10 to 100%) with a fixed pulse duration (10 μs). These data clearly show the gradual transition from narrow, well defined trenches associated with individual SWNTs to uncontrolled flow not correlated to SWNTs.

3.11 Tc-resist Material Selection

Numerous characteristics are critical for an effective Tc-resist material. Basic requirements are that the material can be easily deposited in thin film configurations, where vacuum deposition is preferable to spin-coating, since it easily yields uniform film thickness even in regions near the partial gate electrode structures, where substrate topography is highly nonuniform. The films must afford good coverage and adhesion to both the SWNT and the quartz substrate, and at the same time be sufficiently impermeable to O_2/CF_4 plasma to act as an effective etch resist. The unique chemistry of the Tc-resist material studied here combines hydroxyl and phenyl moieties which provide compatibility with both SWNT and oxide substrates. It is critical for films to exist in an amorphous phase, to avoid spatial nonuniformities in thermal

properties (thermal conductivity, k), viscous flow properties (temperature coefficient of surface tension, γ_1, and viscosity, μ) and thickness that can be associated with crystalline grains. Figure 3.12a,b,c show AFM associated with trench formation experiments with arrays of SWNTs and Tc-resists consisting of thin films of paraffin, TCNQ, and pentacene (similar results were achieved for TCTA and F4-TCNQ). All of these materials show features that roughly correlate to underlying SWNT heaters, but show massive variations in resulting trenches over the area of the film. Films of TAZ and anthracene (deposited at -80 ˚C) yielded amorphous films, but, over the time scales associated with experiments and characterization, exhibited spontaneous crystallization. Other materials, such as polystyrene (MW=288,000, Fig. 3.12d) or Alq3 provided high quality amorphous films, but significantly higher power densities (and/or higher background heating, T_∞ >140 ˚C) were required to yield trenches. (In the case of Alq3, crystallization occurred at lower temperatures than those required for trenches to be observed, in reasonable experimental time scales.) These power densities (or background heating) lead to bias requirements and/or operating conditions in which non-ideal device behaviors (e.g. non-negligible current through the s-SWNTs) limit the selectivity of the TcEP process. Models of thermocapillary flow suggest that such behaviors are due to either low temperature coefficients of surface tension or high viscosities. While both parameters play an important role in the flow (and γ_1 also plays a role in the trench profile), most materials exhibit γ_1 between ~0.05 and ~0.15 mJ/m^2/˚C, while viscosities can vary by many orders of magnitude. It is likely, then, that viscosity is the most significant parameter that determines whether materials yield trenches in experimentally practical time scales and with low power levels, without significant background heating. While the Tc-resist demonstrated here meets all of these criteria, advances could be obtained through the development of materials with similar properties but also suitability for use

at smaller thicknesses (e.g. 5-10 nm, rather than 25 nm). Reductions in thickness enable decreases in W_{Tc} (linearly with h_f) which, in turn, could allow application to arrays of SWNTs with high densities.

3.12 Processes Defined by Critical Temperatures

The unique scaling (particularly power invariance) associated with thermocapillary flow is critical to the success of TcEP, because it allows uniform trenches in arrays of SWNT that incorporate significant variations in power densities among the various SWNTs. Although it is possible to envision approaches like TcEP but which rely on processes such as sublimation or ablation, their robust operation is limited by the existence of a critical temperature, T_C. In such cases, at temperatures below T_C, the resist will remain, while at temperatures above T_C, the film will be removed. Thermal models can provide key insights into the scaling of this type of process. Figure 3.13a,b show temperature profiles and thermal gradients for a range of power densities similar to those measured experimentally. Both peak power and peak gradient scale linearly with power. A width associated with a process that relies on a critical temperature, W_C, can be determined (Fig. 3.13a). Figures 3.13c,d show the predicted scaling for processes associated with critical temperatures of 2-10 ˚C. It reveals that these processes yield no trench until a certain power density is reached. Afterward, the width increases dramatically with increasing power, to widths that would expose other SWNT in arrays of densities >0.1 SWNT/μm. This type of scaling is incompatible with desired operation. For higher T_C the range of powers that yield practical trench widths (several hundred nm) becomes larger. Here, the required power density to initiate trenches grows dramatically, which is also highly undesirable.

3.13 Effects of Trench Formation in Neighboring SWNTs

For very high SWNT densities, non-ideal behavior in TcEP can occur if a trench associated with an m-SWNT exposes an s-SWNT in close proximity. The trench width provides an indicator for the density at which this type of behavior can be expected. In particular, for an array of SWNTs with regular spacing, the maximum density is defined roughly by the average trench width (trench width measured at the base of the Tc-resist ~100 nm, where W_{Tc} is ~250 nm). We note, however, that thermocapillary flow can be altered as neighboring trenches approach one another. At long times the pileups from two adjacent trenches coalesce, creating a narrow strip of Tc-resist in between them. It is unclear from the simple models here, which apply to isolated SWNT, how close the SWNTs can be before their trenches merge. As a result, the minimum spacing between trenches where Tc-resist remains in between them provides the best indicator of the maximum density that can be accommodated in TcEP, as implemented here. AFM measurements of trench formation in arrays with locally high densities suggest that neighboring trenches can be as close as 250 nm while still showing well-defined Tc-resist in between. Figure 3.14 shows an AFM, cross-sectional height profile, and associated 3D renderings of such trenches. Here, isolated trenches are observed along the entire lengths of the trenches (~8 μm).

3.14 Interconnected Arrays of SWNT for Large Area TcEP

For applications where the collections of devices in a target application are known roughly, then it is practical to perform TcEP in local patches, as part of an interconnected array of electrodes. Figure 3.15a shows five 1x5 sets of SWNT processed by TcEP in this manner. Figure 3.15b,c show the transfer characteristics for one of the arrays before and after TcEP and

the characteristics for all five devices after TcEP. For each array, after removing interconnects (lithography and etching), all of the devices (25 total) showed high on/off ratio ($> 1 \times 10^3$). This result demonstrates the effectiveness of performing TcEP over large areas using this type of interconnection scheme.

3.15 Inverter Fabrication and Load Line Analysis

A p-type inverter was fabricated from two devices based on arrays treated by TcEP. Figure 3.16a shows optical micrographs associated with this process. Here, a common source electrode is used to perform TcEP on two arrays with interconnected drain electrodes. Following TcEP, the gate and dielectric layers were removed. For one transistor (the load TFT), the associated source and drain electrodes for TcEP served as electrodes for the final device. For the other (the driver TFT) the source electrode was extended to yield a reduced channel length (~3.5 μm). Finally, new dielectric (SOG/HfO_2, 35/20 nm) and top gate (Ti, 70 nm) structures were defined, to complete the fabrication. The current level for the driver TFT increased roughly linearly with the reduction in channel length from 30 μm to 3.5 μm (expected ratio~8.5, measured ratio~9.5). This current level yielded a current ratio between driver and load TFTs of ~10. Figure 3.16b,c show the electrical properties of the driver and load TFTs. The measured voltage transfer curve (VTC) is consistent with that predicted from load line analysis (Fig. 3.17). Some variation between the measured and predicted VTC curves results from hysteresis in the load and driver TFTs. The measured voltage gain (~4) is near expectation based on the conventional diode-load inverter circuit design equation (~3, $A_V = g_m/g_{m\_load} = (L_{load}/L_{driver})^{0.5}$).[6]

3.16 Mobility Modeling for TcEP Treated SWNTs in Partial Gate Configurations

In order to determine the mobility of devices treated by TcEP, the transfer characteristic from the ~200 s-SWNT (several devices were left out of the analysis because I-V data was over a different range not consistent with averaging) remaining following TcEP were averaged and used as the basis of simulations to establish the average electronic mobility of SWNT treated by TcEP. Self-consistent solutions to the Poisson and drift-diffusion equations[7] were used to simulate partial gate SWNT field-effect transistors (PG-FET) with 1 nm diameter (average diameter expected for populations grown by this technique) s-SWNT as channel. Dimensions of other parameters are based on experiments and shown in Figure 3.18a. Solution of the three-dimensional Poisson equation captures the effect of contact dimensions on the electrostatics of PG-FETs, whereas solution of the drift-diffusion equation describes one-dimensional carrier transport along the s-SWNT. In addition to using analytical expressions for mobility and carrier densities, simulation also considers acceptor doping for s-SWNT to capture the influence of (oxygen and water induced) negatively charged interface defects.

Figure 3.18b shows measured and simulated drain-to-source current (I_{DS}) vs. gate voltage (V_G) characteristics of the PG-FET at different source-drain bias (V_{DS}) for the averaged s-SWNT. The simulation shows good agreement with the values measured under similar bias conditions. (Measured values represent average characteristics for ~30 PG-FETs with ~ 200 s-SWNTs.) The extracted mobility (averaged along the SWNT) is ~ 1050 cm^2/V-sec at VGS ~ 4 V and reduces to ~ 928 cm^2/V-sec at VGS ~ -12 V. Such reduction of mobility at higher VGS is routinely observed in s-SWNT's mobility measurements[8-10] and is related to the increase of average electric field along the SWNT (considered in simulation) and also to the non-parabolicity in

SWNTs band-structure[10] (ignored in simulation). The effect of contact resistance (~ 28 kΩ[8]) is observed to have negligible effect in extracted mobility for the long-channel length PG-FET.

3.17 References

1 Paddock, C. A. & Eesley, G. L. Transient thermoreflectance from thin metal films. Journal of Applied Physics 60, 285-290 (1986).

2 Islam, A. E. et al. Effect of variations in diameter and density on the statistics of aligned array carbon-nanotube field effect transistors. Journal of Applied Physics 111, 054511-054517 (2012).

3 Liao, A., Zhao, Y. & Pop, E. Avalanche-Induced Current Enhancement in Semiconducting Carbon Nanotubes. Physical Review Letters 101, 256804 (2008).

4 Lee, J. et al. Electrical, thermal, and mechanical characterization of silicon microcantilever heaters. J. Microelectromech. Syst. 15, 1644-1655 (2006).

5 Felts, J. R., Somnath, S., Ewoldt, R. H. & King, W. P. Nanometer-scale flow of molten polyethylene from a heated atomic force microscope tip. Nanotechnology 23, 215301 (2012).

6 Wang, C., Zhang, J. & Zhou, C. Macroelectronic Integrated Circuits Using High-Performance Separated Carbon Nanotube Thin-Film Transistors. ACS Nano 4, 7123-7132 (2010).

7 Xie, X. et al. Electroluminescence in Aligned Arrays of Single-Wall Carbon Nanotubes with Asymmetric Contacts. ACS Nano (2012).

8 Zhou, X., Park, J.-Y., Huang, S., Liu, J. & McEuen, P. L. Band Structure, Phonon Scattering, and the Performance Limit of Single-Walled Carbon Nanotube Transistors. Physical Review Letters 95, 146805 (2005).

9 Yang, Z., Liao, A. & Pop, E. Multiband Mobility in Semiconducting Carbon Nanotubes. Electron Device Letters, IEEE 30, 1078-1080 (2009).

10 Perebeinos, V., Tersoff, J. & Avouris, P. Mobility in Semiconducting Carbon Nanotubes at Finite Carrier Density. Nano Letters 6, 205-208 (2006).

3.18 Figures

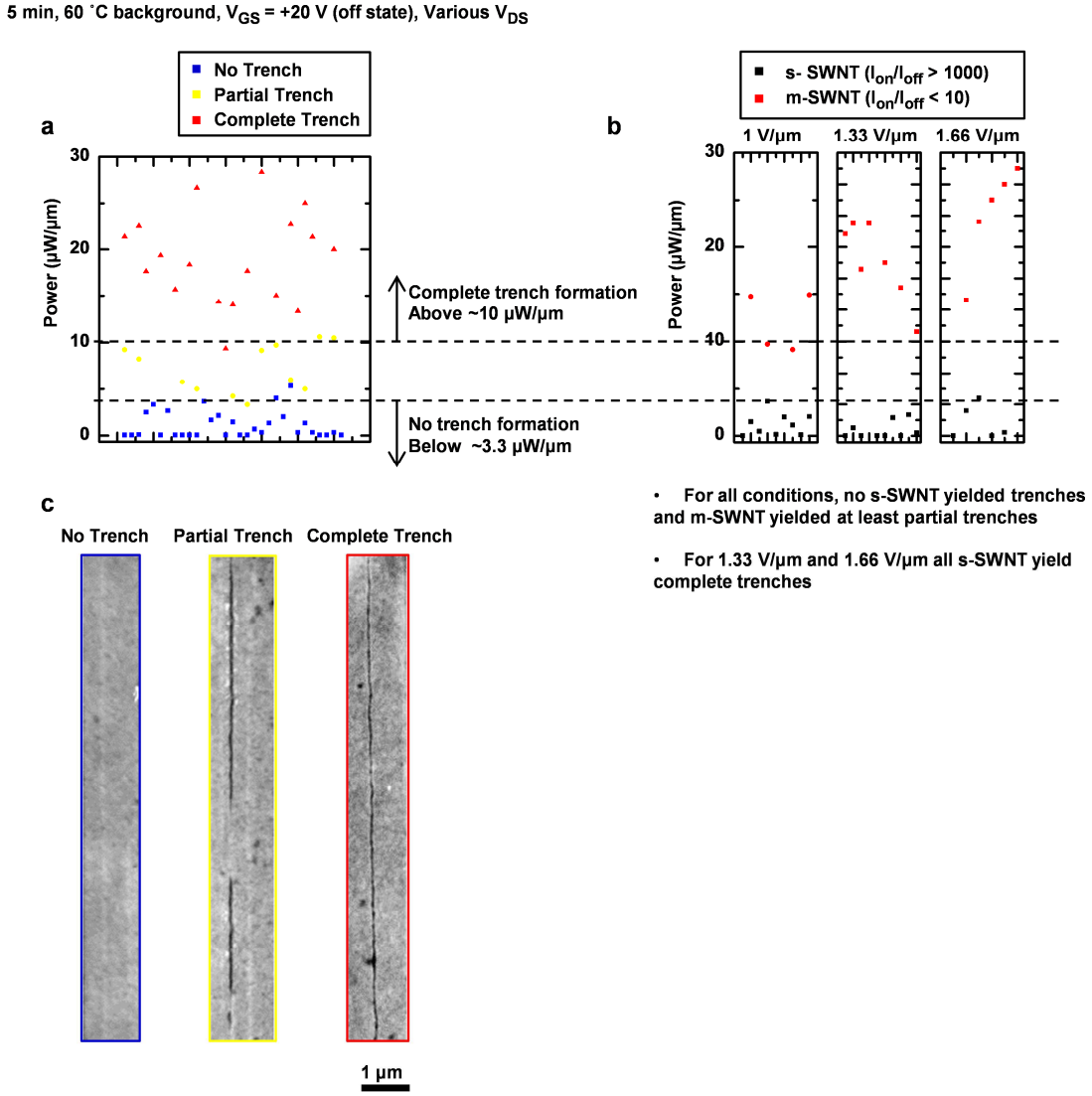

Figure 3.1 Critical power for trench formation. Summary of results on experimental investigations of trench formation (5 min, 60 ˚C) in devices with single or several SWNT, in which an individual SWNT contributed a majority of the current. The findings define the critical power density to form trenches. All experiments were performed with s-SWNT in their "off" state (+20 V_G). (a) Scatter plot of device-level power density associated with the experiments. All devices with power density below 3.3 μW/μm show no trenches (blue), all devices with power density above 10 μW/μm show complete trenches along the entirety of their length (red), while those with intermediate powers show trenches along part of their length (yellow). Here, local variations in resistance along the length of the SWNT yield powers sufficient for trench formation in some, but not all regions of the SWNT. (b) The same set of experiments, organized by source-drain bias and SWNT electronic type. Although there is a large variation in the power associated with various SWNTs at a given bias condition, for optimized conditions (-1.33 and -1.66 V/μm) all s-SWNT exhibit no trenches, while all m-SWNT exhibit complete trenches along their entire length. (c) Representative AFM images for: no trench (left), partial trench (middle), and complete trench (right) formation.

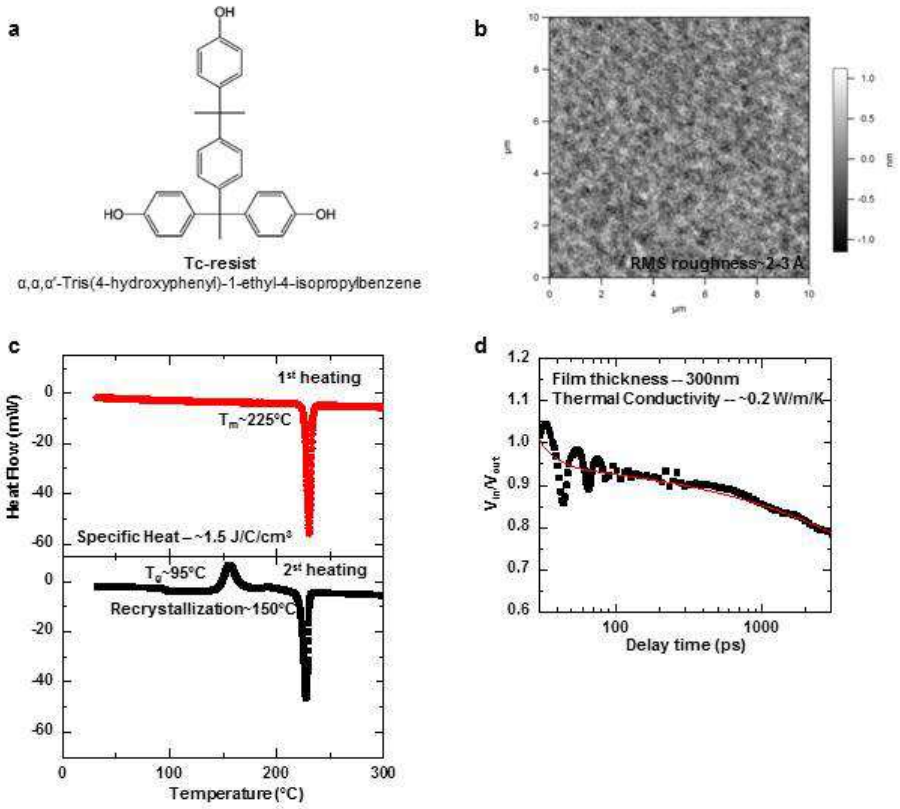

Figure 3.2 Tc-resist characterization. (a) Chemical structure for Tc-resist. (b) AFM of a pristine film deposited by thermal evaporation (25 nm, ~1Å/s) showing a very smooth surface (2-3 Å RMS roughness, similar to underlying Si substrate). (c) DSC of Tc-resist showing specific heat (~1.5 J/C/cm^3), melting temperature (~225 ˚C), recrystallization (~150 ˚C), and glass transition (~95 ˚C) for a bulk sample. (d) Thermoreflectance for a 300 nm thick film of Tc-resist. Fitting yields thermal conductivities of ~0.2 W/m/K.

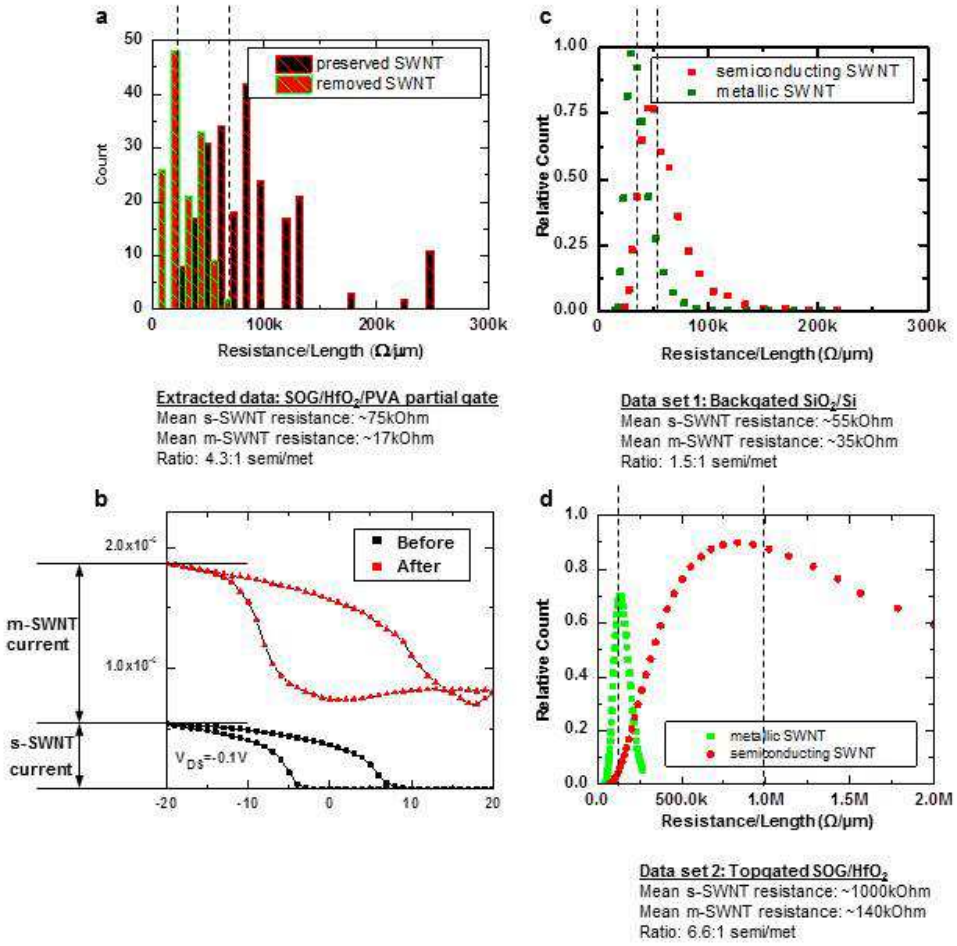

Figure 3.3 SWNT resistivity data. (a) Extracted average resistivity for m-SWNTs and s-SWNTs based on sorted small area arrays. Average resistivity for each of 37 devices based on device resistance changes before and after TcEP and the number of SWNTs removed and remaining (based on AFM). (b) Typical I-V for an array before and after TcEP showing the relative conductance attributed to both m-SWNT and s-SWNT. (c,d) Histograms showing distributions of individual SWNT resistivities for two data sets, one based on back-gated devices on SiO_2/Si and the other based on top-gated devices with a gate dielectric of SOG/HfO_2. Distributions representative of previously published results on arrays of SWNT.

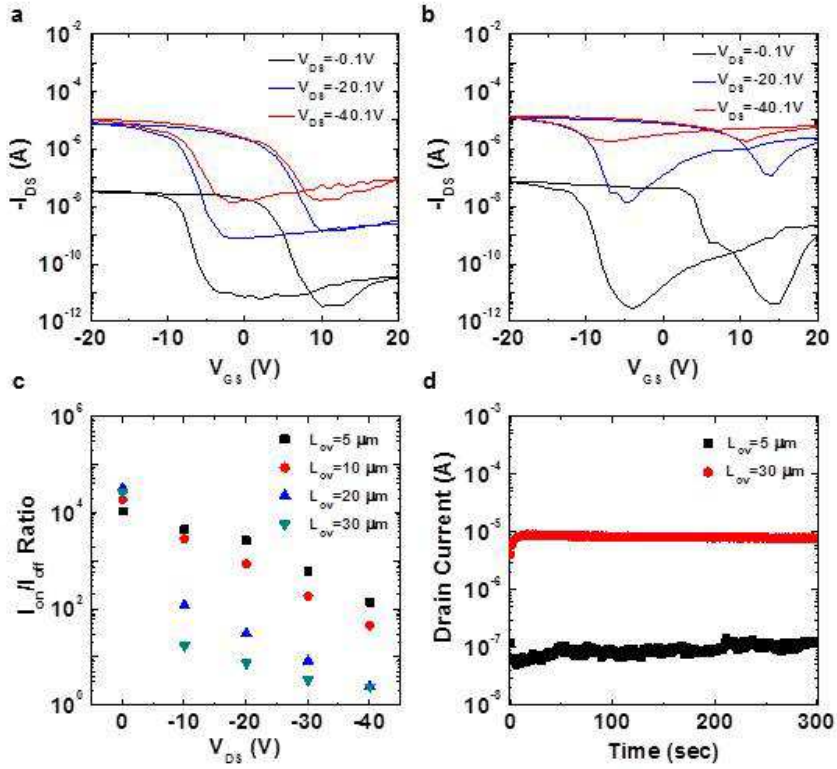

Figure 3.4 Effect of partial gate transistor geometry. Electrical characterization of an individual SWNT device with varying gate overlap. Transfer characteristics for different drain voltages (V_{DS}=-0.1, -20, -40 V) for the case of (a) partial gate and (b) full gate configurations. (c) I_{on}/I_{off} dependence on gate overlap (L_{ov}) ranging from 5 to 30 µm and (d) drain current associated with devices held in their off state (V_{GS}=+20 V) for extended durations, for partial gate and full covered configurations.

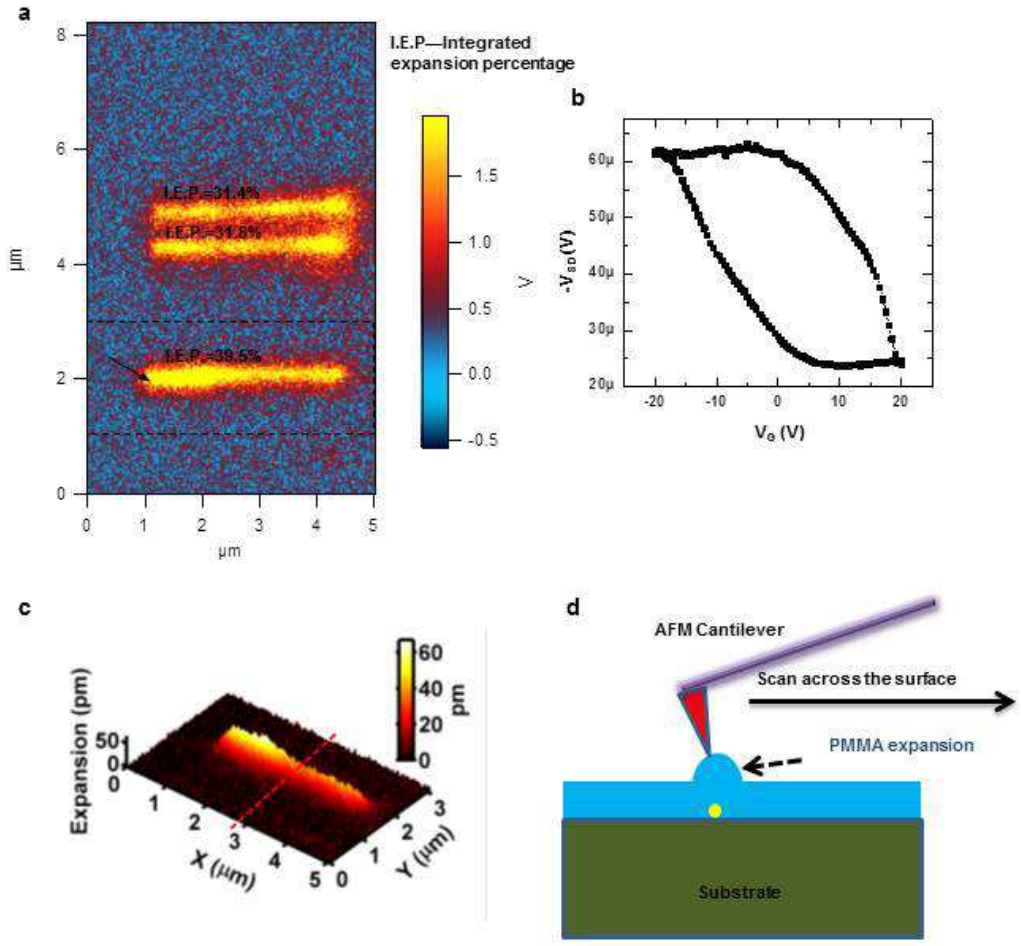

Figure 3.5 Summary of SJEM measurements. (a) Full SJEM image for an array of 3 SWNTs. The relative integrated intensity for each SWNT is indicated. This relative intensity is used to calculate the relative proportion of the total device power density associated with each SWNT. (b) Transfer characteristic of a device with an array of 3 SWNTs. (c) SJEM image for a SWNT used for validation of analytical temperature models (Fig. 2c). (d) Schematic illustration of SJEM measurements.

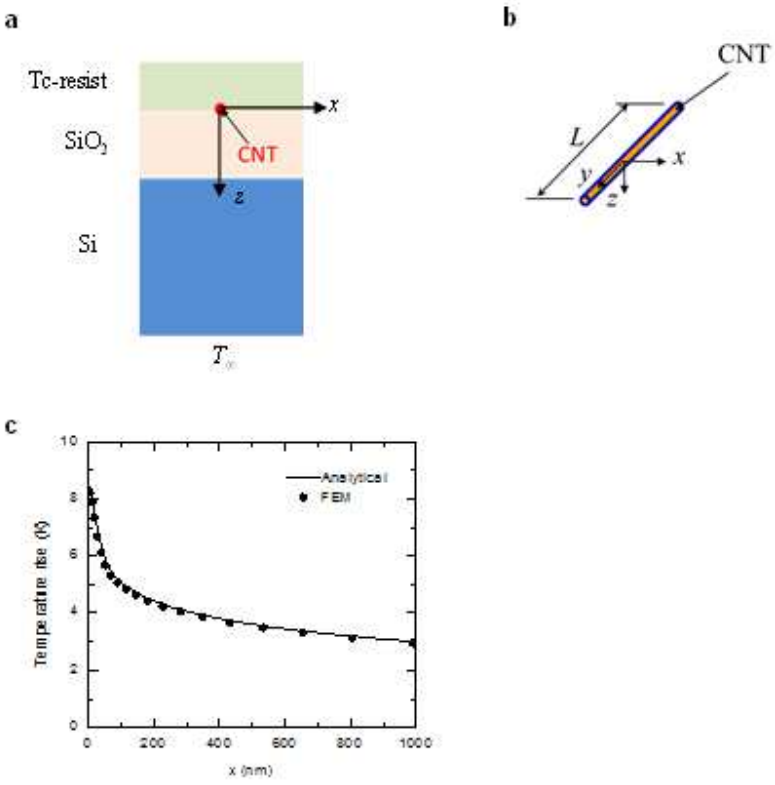

Figure 3.6 Thermal modeling geometry. (a) Cross-sectional schematic of the film and substrate geometry associated with thermal modeling, with axes defined. (b) Modeling axes defined relative to the position of the SWNT. (c) Tc-resist surface temperature distribution for the case of a heated SWNT on a quartz substrate (16.6 μW/μm)

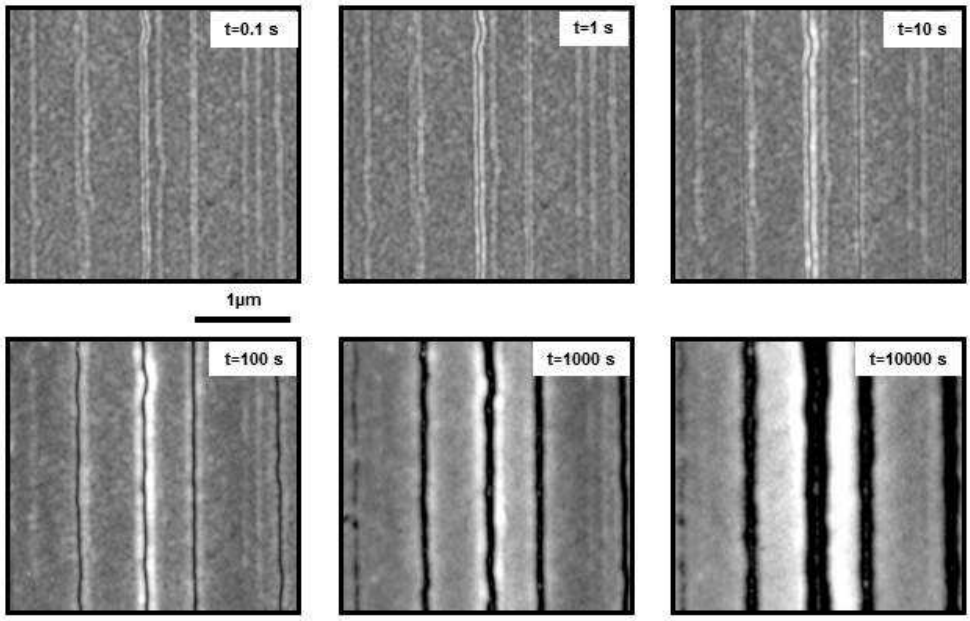

Figure 3.7 Time-dependent trench formation study. 3x3 μm AFM images associated with in-situ measurement of trench formation. Brief intervals of bias were applied and the associated topography was measured (30 s scans) in between each interval. These images are associated with various total accumulated bias durations as trenches evolve.

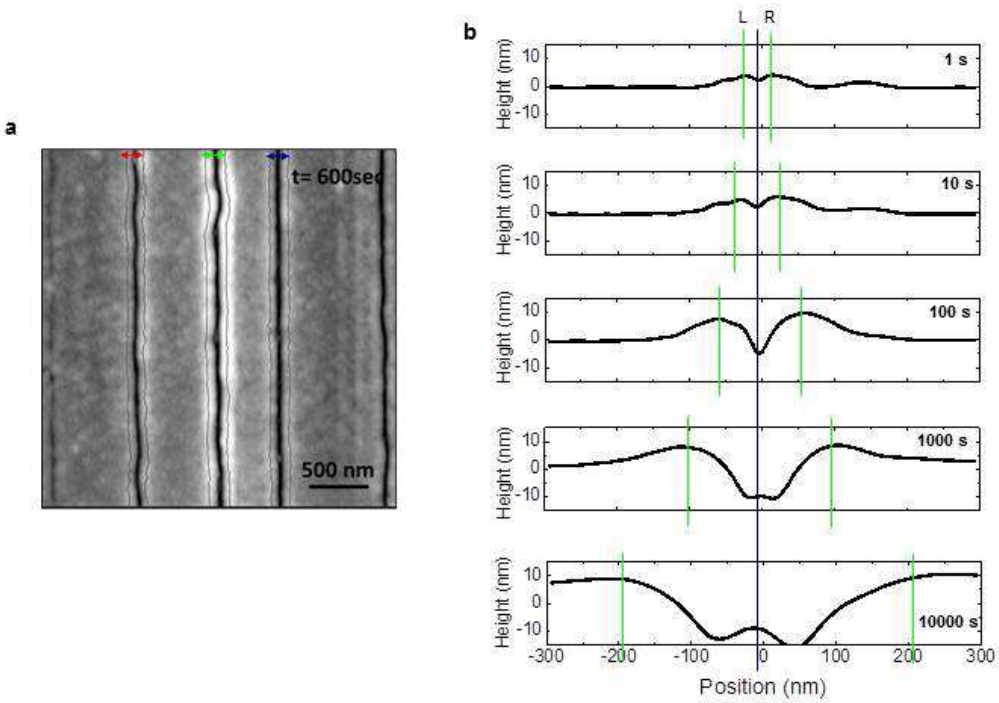

Figure 3.8 Details of trench width identification. (a) Representative image of trench formation. Lines showing the position identified as the right and left trench edge. (b) Representative cross-sectional height profiles at various points in trench evolution. For the purposes of establishing reliable methods of consistently identifying trench width that are independent of AFM tip condition and can yield comparison to features easily identified by thermocapillary flow modeling, the trench edges were associated with the peaks of the pileup on the trench edge. As is evident from the cross-section profiles, that width of the trench at the base is substantially narrower than these values. AFM tip artifacts make precise measurement of this inner width difficult.

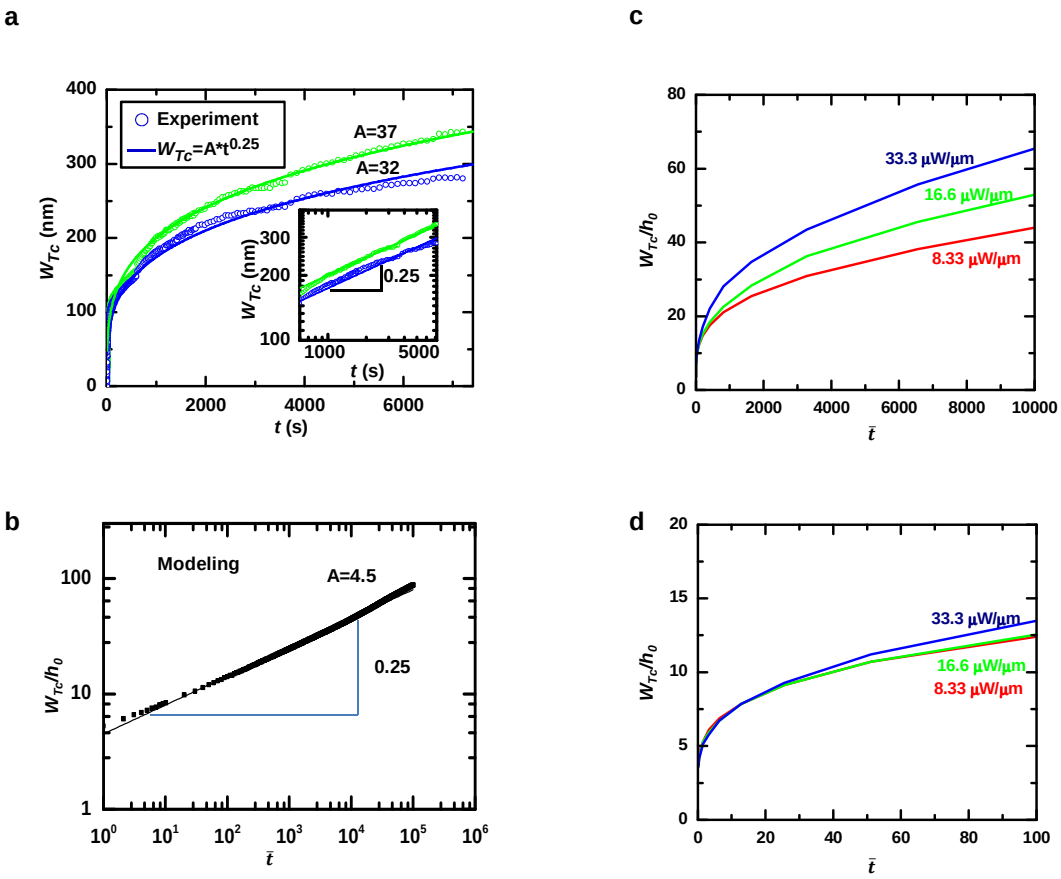

Figure 3.9 Time dependence of trench width. (a) Experimental results showing power law time dependence, with $t^{0.25}$ scaling. Trenches associated with different SWNTs have slightly different prefactors, most likely associated with slight differences in relative power densities. (b) Modeling showing similar $t^{0.25}$ dependence, thus indicating that the model for Tc-flow accurately captures the fundamental scaling of trench formation. (c,d) Time dependence of width for various powers over long and short time scales respectively. For short time scales, where trench widths are comparable to those in TcEP, the width only depends weakly on the power.

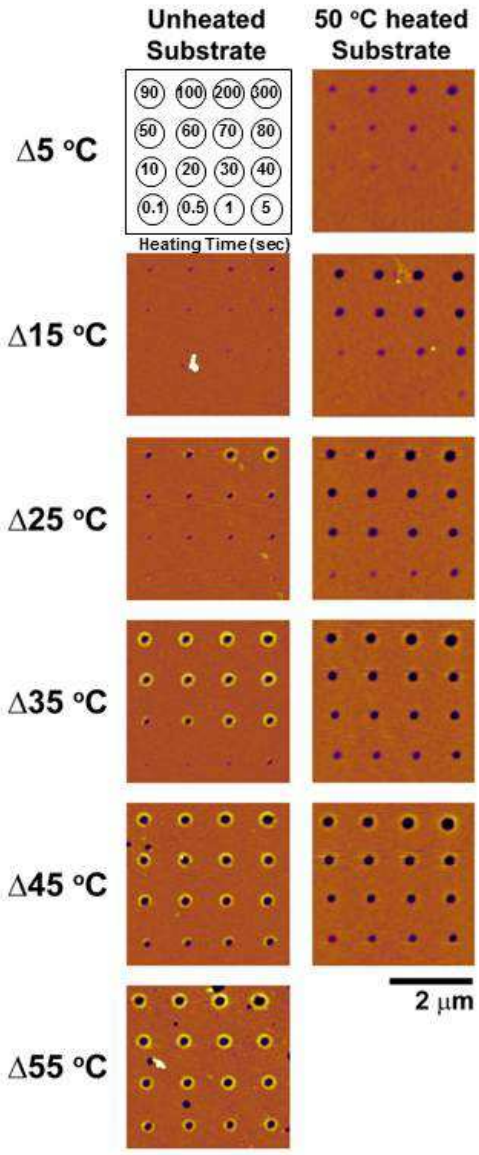

Figure 3.10 Thermocapillary flows in Tc-resist studied with calibrated, heated AFM tips. AFM images of a series of arrays of dots patterned in films of Tc-resist, created by contact of heated AFM tips for a variety of temperature differences (tip to substrate) and contact durations (indicated in first frame) at both room temperature and 60 ˚C. General behavior is consistent with that observed for SWNT Joule heating. In particular, features form in the Tc-resist even at low temperature rises. Feature sizes increase with time.

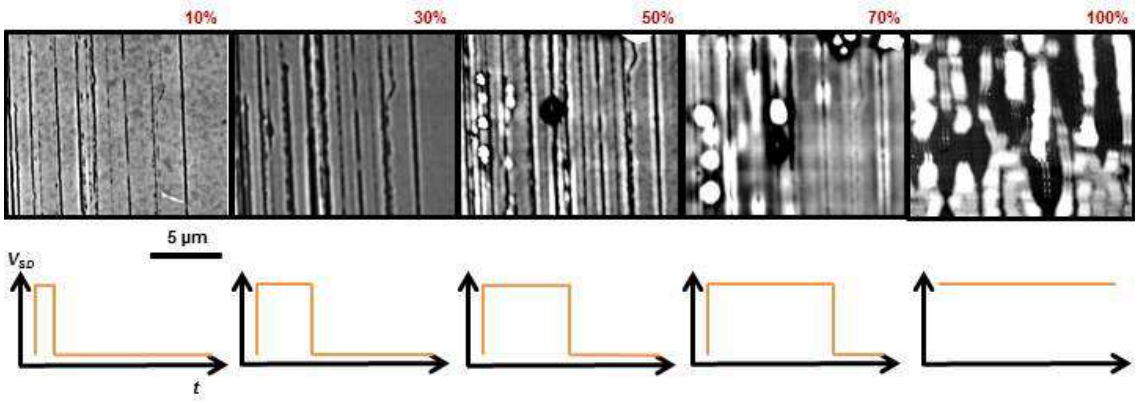

Figure 3.11 Pulsed biases for forming trenches in large and/or high density arrays of SWNTs. AFM trenches formed in Tc-resist for an array with 2-3 SWNT/µm associated with pulsed heating with increasing duty cycle (V_{DS}= -40V peak amplitude, period= 10 µs, duration= 1-10 µs, V_{GS}= +20V DC, 60 sec total stress duration, 50 ˚C background heating). For 10% duty cycle, clearly defined trenches are observed. As the duty cycle increases, trenches become less clearly defined and flow is observed that does not correlate to the underlying SWNT positions. This results from delocalized heating associated with parallel operation in many SWNTs. Pulsed heating aids in localizing the flows needed for proper operation in TcEP.

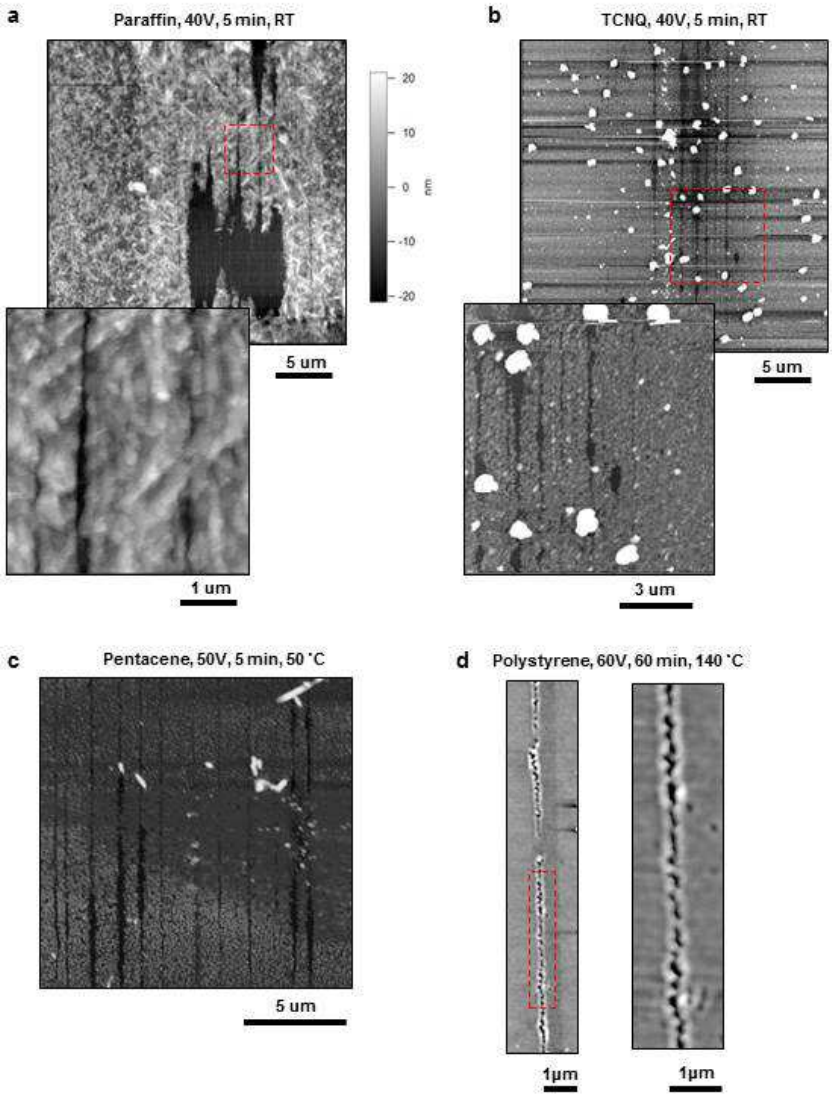

Figure 3.12 Behaviors in other candidate materials for Tc-resists. AFM images of trenches formed for (a) paraffin, (b) TCNQ, and (c) pentacene. Some trenches are observed, but with non-uniform widths. For these materials, such behaviors can be attributed to their morphology. Other materials explored, such as polystyrene (d), failed as Tc-resists due to inability to form trenches at sufficiently low powers (likely due to high viscosity or low temperature coefficient of surface tension) and/or insufficient etch resistance.

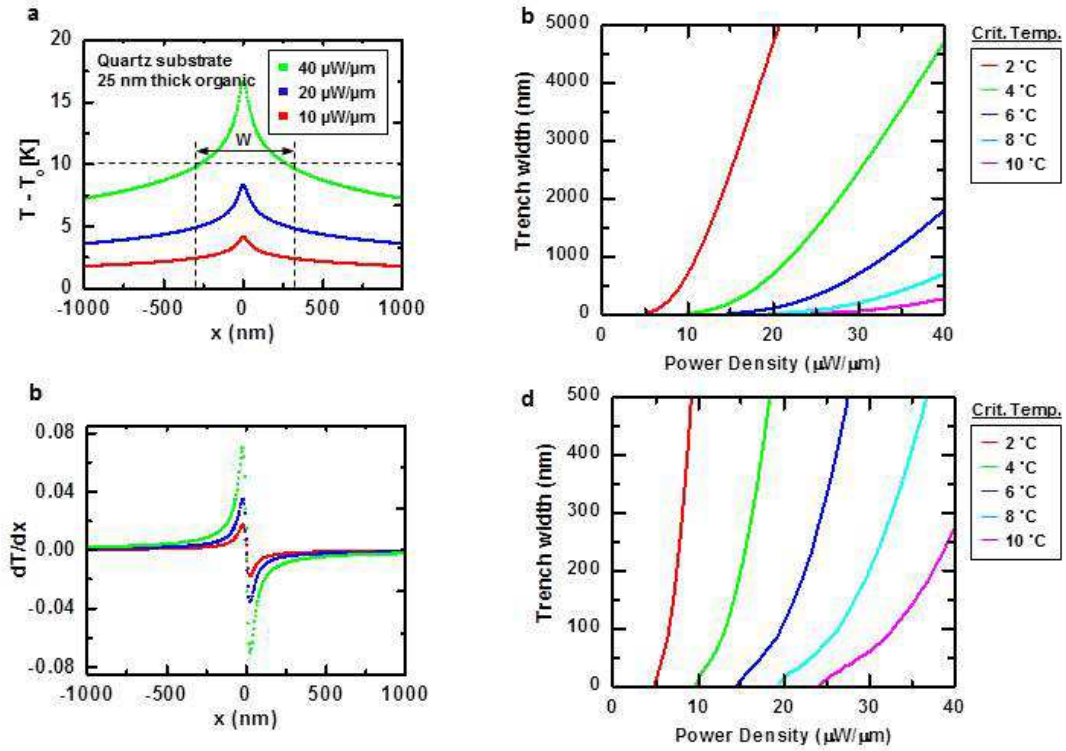

Figure 3.13 Theoretical trench width for processes based on critical temperatures. (a,b) Temperature profiles and gradients predicted by analytical thermal models for a variety of powers. Processes such as sublimation or ablation have a critical temperature associated with them such that all material at or above this temperature is removed and all below the critical temperature is preserved. (c,d) Power dependence of predicted trench width associated with processes with critical temperatures ranging from 2-10 ˚C. Processes with higher critical temperature should show similar scaling but with higher power density required to yield trenches (unsuitable for TcEP). This type of scaling is not ideal for TcEP, since at conditions sufficient to yield trenches in the least conductive m-SWNT, the most conductive SWNTs would exhibit very wide trenches (several µm), thereby exposing neighboring SWNTs.

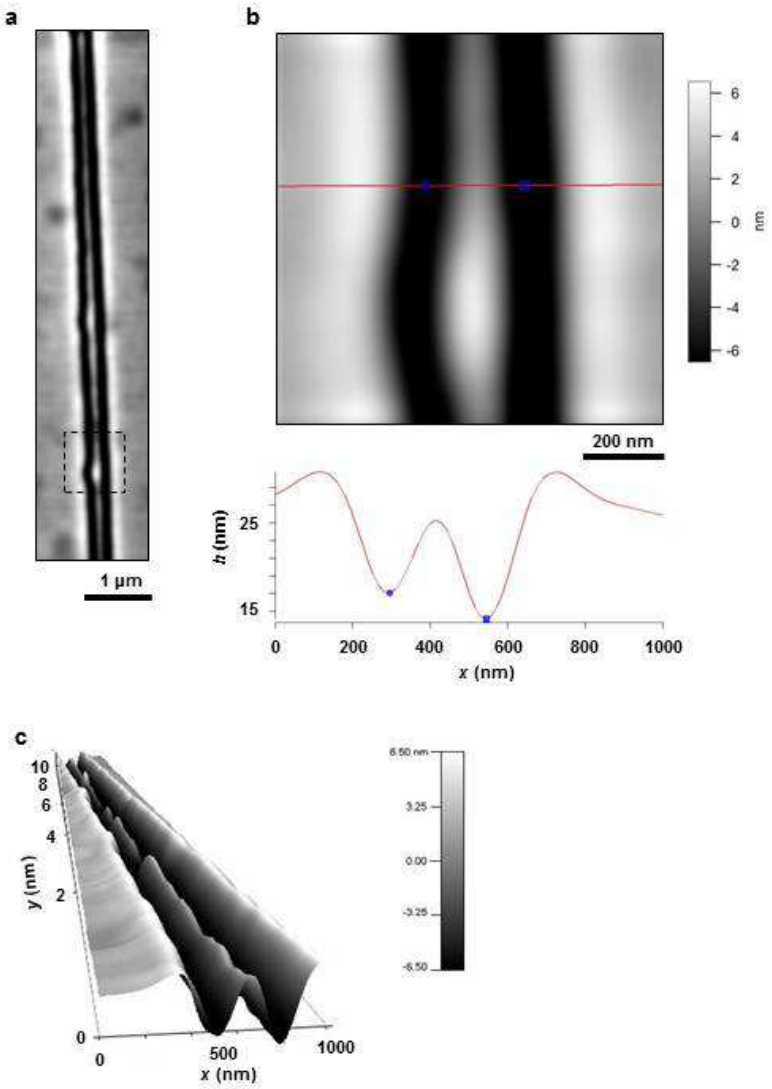

Figure 3.14 Trenches in cases with neighboring SWNTs. AFM images associated with two distinct trenches that form from heating in neighboring SWNTs. Despite their close proximity (250 nm) two distinct trenches form along the lengths of the SWNTs (~10 µm).

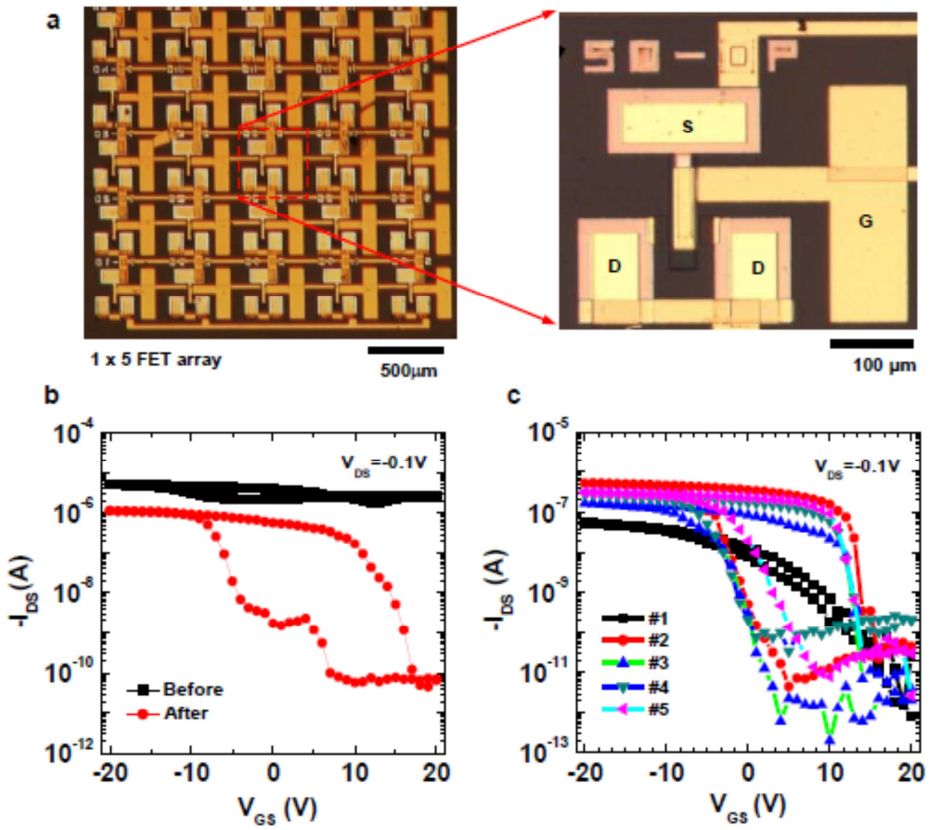

Figure 3.15 Details of TcEP in a parallel operational mode. (a) Optical images for a 1 X 5 array of SWNT arrays and associated electrodes for TcEP, with electrodes connected in parallel (b) transfer characteristics before and after TcEP in parallel and (c) transfer characteristics for disconnected individual arrays following TcEP. All arrays show high on/off ratio following TcEP.

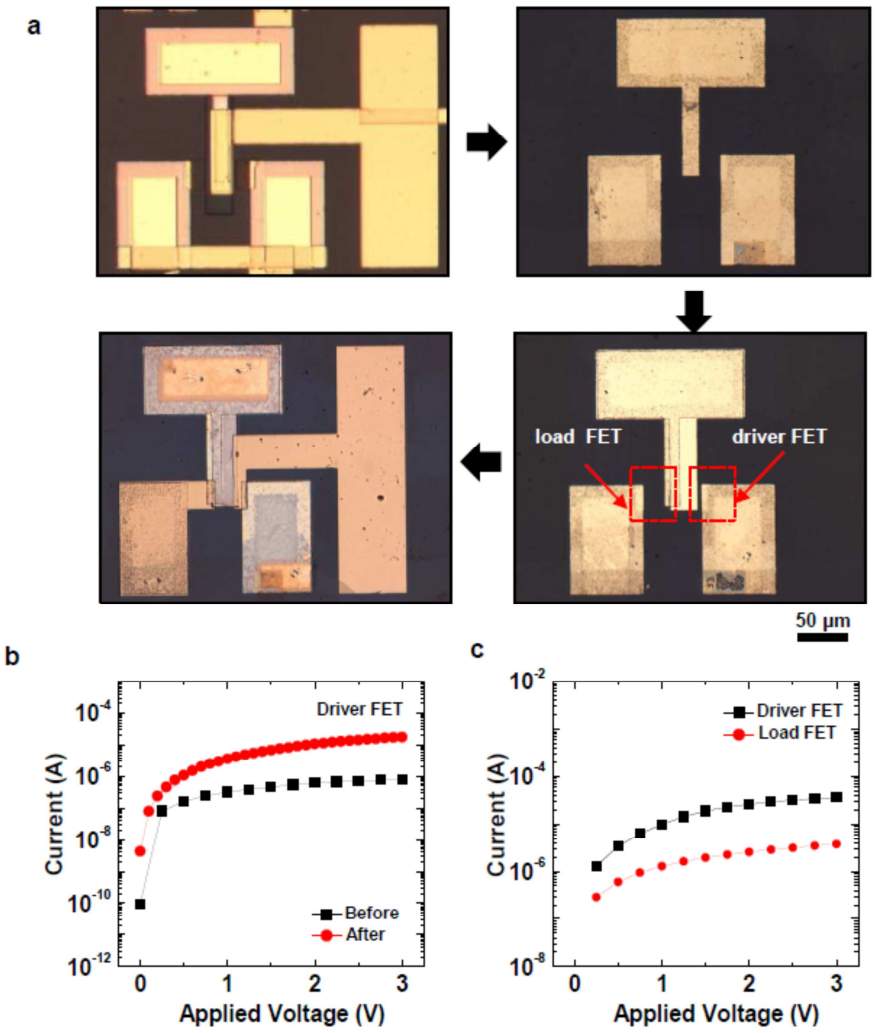

Figure 3.16 Details of inverter fabrication. (a) Optical micrographs of process flow for inverter fabrication. TcEP was performed on two arrays in parallel, the gate electrode and dielectric layers were removed, and then new, top-gated TFTs were fabricated with appropriate channel lengths for optimal inverter performance. (b) I-V characteristics of driver FETs associated with electrodes used for TcEP (30 µm channel length) and final device configuration (3.5 µm channel length), respectively. (c) I-V characteristics of driver and load TFTs following inverter fabrication.

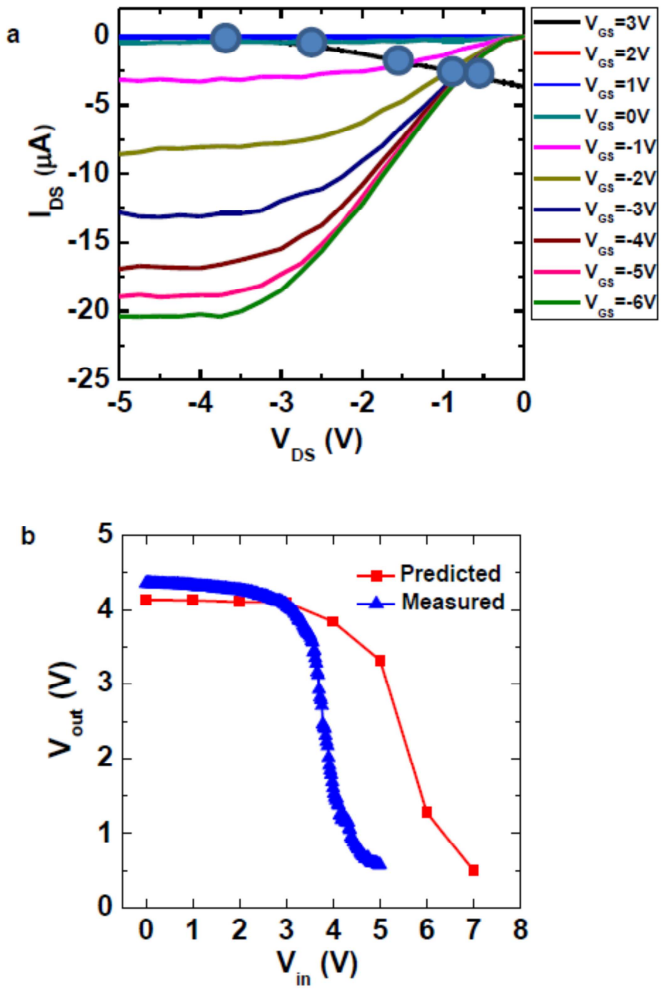

Figure 3.17 Inverter fabricted using arrays processed by TcEP. (a) load line analysis for the inverter and (b) voltage transfer characteristics measured and predicted from load line analysis

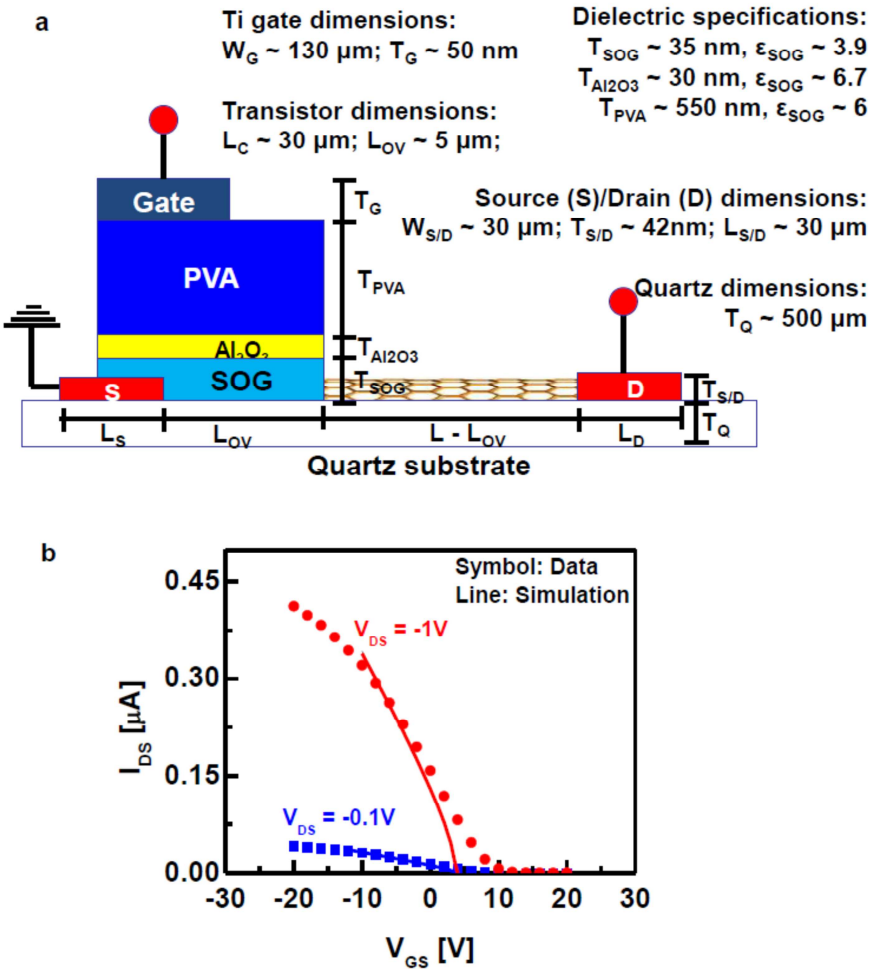

Figure 3.18 Mobility calculations for TcEP treated devices in partial gate geometry. (a) Cross-sectional schematic of a PG-FET geometry used for modeling (based on experiment) of Ti/Pd source/drain, Ti gate, and PVA/Al_2O_3/Spin-on-glass (SOG) dielectric. Values for width (W), length (L) and thickness (T) of different components of PG-FET are also specified. (b) Measured drain to source current (I_{DS}) vs gate to source bias (V_{GS}) averaged over ~ 35 TcEP treated PG-FETs with ~200 s-SWNTs at two different drain to source bias (V_{DS}). Simulation of PG-FET by considering the dimensions specified in Figure (a) and using ~ 1 nm diameter s-SWNT as channel matches the measured data and suggests ~ 928-1050 cm^2/V-sec (smaller mobility for larger V_{GS}) as the device mobility at different bias conditions.

CHAPTER 4: CONCLUSION

In this work, we studied fundamental aspects of this alignment process and developed a post-growth treatment, TcEP, which allows for highly selective and scalable purification of these arrays. We believe that the scalable nature of this approach should create a route for circuit scale demonstrations in the future.

The electrode geometries associated with TcEP are not ideal; however, the basic principle of TcEP centers around the use of induced heating in SWNT to pattern thin organic layers and the scaling and physics associated with this process. Regardless of how heating is induced, this basic scheme provides the practical benefit of reducing the power for removal significantly and providing complete physical removal. Overall, we believe that the research presented here represents a significant step towards the goal of perfectly aligned arrays of s-SWNTs.